Applied Mathematical Modelling 40 (2016) 7474–7492

Contents lists available at ScienceDirect

Applied Mathematical Modelling

journal homepage: www.elsevier.com/locate/apm

Particle diffusion in non-equilibrium bedload transport simulations☆

Patricio Bohorquez[a,*], Christophe Ancey[b]

[a] Área de Mecánica de Fluidos, Departamento de Ingeniería Mecánica y Minera, CEACTierra, Universidad de Jaén, Campus de las Lagunillas, 23071 Jaén, Spain
[b] Environmental Hydraulics Laboratory, École Polytechnique Fédérale de Lausanne, Lausanne 1015, Switzerland

ARTICLE INFO

Article history:
Received 29 June 2015
Revised 21 March 2016
Accepted 29 March 2016
Available online 8 April 2016

Keywords:
Saint-Venant–Exner equations
Particle diffusion
Adaptation length
Bed degradation
Anti-dunes

ABSTRACT

This paper examines the importance of particle diffusion relative to advection in bedload transport. Particle diffusion is not included in existing approaches to bedload transport. Based on recent advances in the probabilistic theory of sediment transport, this paper emphasizes the part played by particle diffusion in bedload transport. The proposed model consists of the classic Saint-Venant–Exner equations supplemented by an advection–diffusion equation for particle activity (solid volume of particles in motion per unit streambed area). The model is solved numerically using standard finite-volume techniques. Our numerical simulations consider two case studies: (i) bed degradation under subcritical flow conditions and (ii) anti-dune development in supercritical flows on sloping gravel beds. These simulations show that particle diffusion plays a key role in bedload transport under non-uniform flow conditions. The diffusive sediment transport rate may be as large as the advective transport rate. When anti-dunes develop and migrate upstream, particle diffusion can create fluctuations in the sediment transport rate, whose amplitude compares with the capacity transport rate. Non-uniform flows can be characterized by a typical length, referred to as the *adaptation length*, which represents the distance that a particle dislodged from the bed travels before it reaches steady-state velocity. We show that the adaptation length is controlled by the particle advection velocity, particle diffusivity, and entrainment/deposition rates, but is independent of the bedform wavelength (contrary to common belief). For simulating bed degradation and anti-dune migration in gravel-bed rivers, a benchmark analysis of different bedload transport models provides evidence that those including particle diffusion perform better than classic models.

1. Introduction

In bedload transport theory, the prevailing view has long been that particles are advected by the water flow. This stimulated approaches which are now routinely used for simulating sediment transport over short time-scales (*e.g.*, floods) [1]:

(i) In the classic approach, hereafter referred to as *equilibrium transport theory*, the sediment transport rate q_s is defined as a conditional function of the Shields number $Sh = \tau_b/(\Delta\varrho g d)$, with τ_b the bottom shear stress, $\Delta\varrho$ the density

☆ This article belongs to the Special Issue: SI: ANMH 2015.

* Corresponding author. Tel.: +34 953211872; fax: +34 953212870.
E-mail addresses: patricio.bohorquez@ujaen.es (P. Bohorquez), christophe.ancey@epfl.ch (C. Ancey).

http://dx.doi.org/10.1016/j.apm.2016.03.044

mismatch between fluid and sediment, g the gravitational acceleration, and d the mean particle diameter. The function is *conditional* because the Shields number must be greater than the critical value Sh_{cr} (threshold of incipient motion) for the solid discharge to be nonzero: $q_s = f(Sh)$ for $Sh > Sh_c$, but $q_s = 0$ for $Sh \leq Sh_{cr}$. The relation $q_s = f(Sh)$ also implies that the sediment transport rate is a one-to-one function of the water discharge (or, equivalently, the bottom shear stress or shear velocity) independently of the flow conditions (*i.e.*, for steady as well as unsteady non-uniform flows) provided that $Sh > Sh_{cr}$. Many bedload transport equations derived empirically (*e.g.*, Meyer-Peter and Müller [2], Ackers and White [3], Parker [4]) are commonly used and provide decent predictions at sufficiently high Shields numbers and over long time-scales [5]. When embodied in the Exner equation, these equations also dictate bed evolution.

(ii) The alternative approach, hereafter referred to as *non-equilibrium transport theory*, is rooted in Einstein's pioneering work [6]. In Einstein's view, sediment transport results from the imbalance between the entrainment and deposition rates. Thus, the sediment transport rate is not uniquely defined by the Shields number but adjusts to the flow conditions. One might expect there to be an evolution equation for q_s which describes its time variation depending on the flow conditions. Indeed, a steady state is reached in a domain at a certain distance beyond the system boundaries and/or once a certain time has elapsed from the initial state, and so there is a domain for which sediment transport is out of equilibrium. The question arises of how to characterize the dimensions of this domain. Authors introduced the *adaptation length* (also called the relaxation or saturation distance) as an additional parameter representing the typical distance that a particle dislodged from the bed travels before it reaches steady-state velocity [7–9]. Non-equilibrium transport theory has recently attracted growing attention, especially in the context of rapidly varying flows, *e.g.*, sediment-laden flows with various sediment transport modes [10,11], erodible dam-break flows [12–15], aggradation due to overloading and degradation by overtopping flow [14,16,17], turbidity currents [18], sediment budget estimation [19], and cyclic steps [20].

It is noteworthy that none of these approaches considers diffusion to be a key process of sediment transport over short time-scales. However, there are many reasons why the role played by diffusion should be reconsidered. Firstly, experiments have highlighted the diffusive nature of bedload transport [21–27]. Particle tracking led to diffusivity in the $0.007 - 0.04$ m^2 s^{-1} range [28,29], whereas other techniques based on the spread of particle clouds showed diffusivity to be lower, ranging from 2.6×10^{-4} m^2 s^{-1} to 4.6×10^{-4} m^2 s^{-1} [30,31]. Secondly, for hillslope sediment transport occurring over long time-scales (soil creep over many years, landscape dynamics over centuries), diffusion is usually the prevailing transport process [32–36]. To fill the theoretical gap, new theories incorporating diffusion have been developed in recent years. They have provided evidence that particle diffusion gives rise to fluctuations in the particle transport rate q_s and *particle activity* γ (solid volume of particles in motion per unit streambed area) [37,38]. Strikingly, theory also shows that particle advection produces nonlocal effects, which look like (local) diffusion on the macro-scale, with a pseudo-diffusivity depending on the scale of analysis and particle velocity [39].

This paper examines the part played by particle diffusion in bedload transport. To do so, it uses a simple one-dimensional morphodynamic model consisting of the Saint-Venant–Exner equations. These equations are supplemented by an advection–diffusion equation that describes the dynamics of sediment transport and is a continuation of the authors' earlier developments [38,40]. One key feature of this approach is that it sheds new light on non-equilibrium bedload transport theory; it thus allows us to revisit the concept of adaptation length. More specifically, our approach shows how the adaptation length depends on the mean sediment velocity $\bar{u}_s$ (the velocity of particles carried by the stream), particle diffusivity D_u, and the erosion/deposition rate κ [25]. This contrasts with non-equilibrium bedload transport models, in which the modeler prescribes the adaptation length and transport capacity using empirical relationships (the numerical outputs are therefore very sensitive to the modeler's choices, as shown by Zhang and Duan [41] and Wainwright et al. [42]). The present paper shows how transport capacity can be determined for Shields numbers in the range of 0–0.3, *i.e.*, from vanishingly low transport rates to a full mobility regime, but below the threshold of sheet flow and suspended load [43]. This paper also shows how useful the dimensionless Péclet number $Pe = \bar{u}_s/\sqrt{D_u \kappa}$ is in estimating the influence of diffusive transport on total bedload transport (compared to advective transport).

The paper is organized as follows. Section 2 recaps the governing and closure equations derived in our earlier publications [38,40]. Section 3 revisits the concept of adaptation length and shows numerical solutions to our governing equations. We study the geometry of a flume, with a focus on (i) bed degradation – a standard in any benchmark numerical simulations – and (ii) anti-dune migration. These two scenarios are representative of shallow, nearly one-dimensional water flows over erodible gravel beds (more complex bedforms, such as alternate bars, are not investigated). Aside from its practical benefits in engineering, we use bed degradation as an example with which to estimate the significance of diffusive bedload transport relative to advective transport under gradually varying flow conditions. Our simulations can be compared with Newton's experiments [44]. The second scenario tests our model's capacity to produce regular bed patterns, such as anti-dunes. More specifically, the test can be considered successful if, starting from an initially planar bed condition, the model predicts bed instability and properly self-selects the anti-dune wavelength. For this scenario, the model's performance can be evaluated by comparing numerical simulations with experimental data [45–48]. For both scenarios, we show that particle diffusion is a key process. Numerical simulations further suggest that the convective and diffusive transport rates are of comparable magnitude when bedforms develop along the streambed. To the best of our knowledge, this is the first time that this remarkable feature has been reported. Section 4 comments on the similarities and differences between our model and existing equilibrium and non-equilibrium bedload transport models. Finally, our conclusions are presented in Section 5.

2. Governing equations

We previously developed a model referred to as the *stochastic Saint-Venant–Exner* (SVE) equations [40], but here we use an ensemble-averaged formulation. This formulation consists of four coupled equations. The first three describe water flow over a sloping erodible bed; the fourth is related to sediment transport. For the sake of simplicity, the flow is assumed to be one-dimensional. A coordinate system $Oxyz$ is defined with the x-axis pointing in the horizontal direction, the z-axis across the flow, and the y-axis pointing in the vertical direction. Water flows in the x-direction.

2.1. Momentum and mass conservation for water and mass conservation for the bed

The first two equations are the shallow water equations (also called the Saint-Venant equations) that express the mass and momentum conservation of the water flow; these are supplemented by the Exner equation tracking the bed-stream interface [49]:

$$\frac{\partial h}{\partial t} + \frac{\partial h\bar{v}}{\partial x} = 0, \tag{1}$$

$$\frac{\partial h\bar{v}}{\partial t} + \frac{\partial h\bar{v}^2}{\partial x} + gh\frac{\partial h}{\partial x} = -gh\frac{\partial y_b}{\partial x} - \frac{f\,\bar{v}\,|\bar{v}|}{8} + \frac{\partial}{\partial x}\left(\nu h\frac{\partial \bar{v}}{\partial x}\right), \tag{2}$$

$$(1-\zeta_b)\frac{\partial y_b}{\partial t} = D - E, \tag{3}$$

in which $h(x,t) = y_s - y_b$ denotes the flow depth with $y_b(x,\ t)$ [m] and $y_s(x,\ t)$ [m] the bed and free surface elevations, respectively, $\bar{v}$ [m s^{-1}] is the depth-averaged velocity, t [s] is time, f is the dimensionless Darcy–Weisbach friction factor, ζ_b is the bed porosity, D [m s^{-1}] and E [m s^{-1}] represent the deposition and entrainment rates, respectively, and the extra term $\partial_x(\nu h\partial_x\bar{v})$ represents a depth-averaged Reynolds stress. A rough estimation of the eddy viscosity is given by $\nu \approx \nu_t h v\sqrt{f/8}$ [m^{2}s $^{-1}$] with the dimensionless parameter ν_t in the 4–18 range [40,50]. Empirical closure equations are used for f, E, and D:

- The Darcy–Weisbach friction factor f is assumed to be a nonlinear function of the relative grain roughness $\delta^2 = d/h$ with d as the mean particle diameter [51]. For a fully developed turbulent flow and a rough regime, we use the Colebrook equation:

$$\frac{1}{\sqrt{f}} = -2\,\log\left(\frac{k_s\,\delta^2}{3.71}\right), \tag{4}$$

  in which k_s is a scaling factor requiring calibration to account for sidewall effects, form drag, and flow recovery [51]. Thus, the local Shields number reads:

$$Sh = \frac{f\,Fr^2}{8\,(s-1)\,\delta^2} \quad \text{with} \quad Fr = \frac{|\bar{v}|}{\sqrt{gh}}, \tag{5}$$

  where s represents the sediment-to-liquid density ratio (typically $s = 2.65$ for gravel in water) and Fr denotes the Froude number.
- The deposition and entrainment rates are linear functions of the mean particle activity:

$$D = \sigma\,\langle\gamma\rangle \quad \text{and} \quad E = \lambda + \mu\,\langle\gamma\rangle, \tag{6}$$

  where $\langle\gamma\rangle$ is the mean particle activity (the angular brackets $\langle\cdot\rangle$ denote the ensemble average). σ, λ, and μ are the particle deposition, entrainment, and collective entrainment coefficients, respectively. The linear structure of these relationships is a key assumption of the stochastic model [38,39,52]. Little is known about the dependence of these coefficients on the flow variables. Experiments conducted by Ancey et al. [52] showed that λ and σ vary almost linearly with $\bar{v}$, whereas μ is nearly constant for the flow range explored.

2.2. Mass conservation for bedload

Bed load transport is described using the following advection–diffusion equation:

$$\frac{\partial}{\partial t}\langle\gamma\rangle + \frac{\partial}{\partial x}(\bar{u}_s\,\langle\gamma\rangle) - \frac{\partial^2}{\partial x^2}(D_u\langle\gamma\rangle) = E - D\,, \tag{7}$$

where $\langle\gamma\rangle$ is the mean particle activity [m], D_u [m^2 s^{-1}] is the particle diffusivity, and $\bar{u}_s = \beta\,\bar{v}$ [m s^{-1}] is the mean velocity of moving particles, with β given by Bohorquez and Ancey [40]:

$$\beta \equiv \min\left(1.44\sqrt{\frac{f}{8\,Sh_{cr}}}, 1\right). \tag{8}$$

Eq. (7) is a deterministic partial differential equation that is obtained by taking the ensemble average of Eq. (A.1) (see Appendix A). It describes how the number of moving particles (per unit streambed area) varies with time as a result of advection by the water flow (at velocity $\bar{u}_s$), spread along the x-axis, and entrainment or deposition depending on the sign of $E - D$. This equation reveals how many particles are moving, but it does not tell us much about the particle transport rate. To answer this point, we need a clear definition of the particle transport rate.

Unfortunately, there is no unique definition of the sediment transport rate [53–55]. Here, we follow Furbish et al. [37] and define the mean sediment transport rate (per unit width of the flow) $\bar{q}_s$ as the sum of convective and diffusive contributions:

$$\bar{q}_s = \bar{u}_s\langle\gamma\rangle - \frac{\partial}{\partial x}(D_u\langle\gamma\rangle)\,. \tag{9}$$

In subsequent sections, we will refer to the *advective transport rate* as $\bar{q}_{c,s} = \bar{u}_s\langle\gamma\rangle$ and to the *diffusive transport rate* as $\bar{q}_{d,s} = -\partial_x D_u\langle\gamma\rangle$. Both contributions can be computed by solving the advection–diffusion equation (7) for the mean particle activity $\langle\gamma\rangle$.

2.3. Steady state solutions

Steady state solutions are not only important for characterizing the system's behavior, but they are also useful in stability analysis (see Section 3.3). Let us consider a steady uniform flow down a sloping bed with constant bottom slope $-\partial_x y_b = \tan\theta$ and with a constant water discharge Q (per unit width). The solution to the Saint-Venant–Exner Eqs. (1)–(3) is straightforward: $h = H,\ \bar{v} = V,\ y_b = -x\tan\theta,$ where H denotes the flow depth, and V is the flow depth-averaged velocity. The flow variables H and V are the implicit solutions to the dimensionless relation reflecting the balance between the gravitational forces and flow resistance in Eq. (2):

$$\tan\theta = \frac{f\,V^2}{8\,gH} = \frac{f}{8}\,Fr^2, \tag{10}$$

where $Fr = V/\sqrt{gH}$ denotes the Froude number. Under steady-state planar-bed conditions, the Shields number (5) achieves the constant value:

$$Sh = \frac{\tan\theta}{(s-1)\,\delta^2}\,. \tag{11}$$

The steady-state particle activity $\langle\gamma\rangle_{ss}$ reflects the balance between deposition and entrainment ($E = D$) in Eq. (7):

$$\langle\gamma\rangle_{ss} = \frac{\lambda}{\kappa} \quad \text{with} \quad \kappa = \sigma - \mu. \tag{12}$$

The steady-state sediment transport rate is:

$$\bar{q}_{ss} = \bar{u}_s\,\langle\gamma\rangle_{ss} = \beta\,\bar{v}\,\frac{\lambda}{\kappa}\,. \tag{13}$$

In Appendix B, we show how the empirical bedload transport equation $\bar{q}_{ss}(Sh)$ developed by Fernandez Luque and van Beek [56] can be extended to cover a wide range of flow conditions, and we use this extended equation in our computations.

Note that neither the steady-state particle activity $\langle\gamma\rangle_{ss}$, nor the steady stage $\bar{q}_{ss}$ are influenced by particle diffusion.

3. Results

This section focuses on the two following issues: (i) we show how the concept of *adaptation length* fits in with SVE Eqs. (1)–(3) and (7) (see Section 3.1), and (ii) we analyze the importance of particle diffusion relative to particle advection in two different case studies, which also serve to benchmark the numerical results against experimental and theoretical solutions. Section 3.2 is devoted to the simulation of a degrading bed, whereas Section 3.3 gives a numerical study of anti-dune migration along gravel streambeds over a steep slope.

As the numerical implementation has been detailed previously and at length in [40,57], we will not dwell on this issue. However, a summary explanation is needed. A fractional-step method was applied to split the advection–diffusion Eqs. (1)–(3) and (7) into a hyperbolic subproblem with source terms and a parabolic subproblem. The hyperbolic subproblem was solved numerically using a fifth-order accurate, weighted essentially nonoscillatory (WENO) scheme, a second-order-accurate, source term discretization, and a third-order accurate, strong stability preserving (SSP), Runge–Kutta time integration – denoted by SSPRK (3,3) in [58]. The eddy and particle diffusivity terms were integrated with the one-step implicit Crank–Nicholson scheme, which is second-order accurate in space and time.

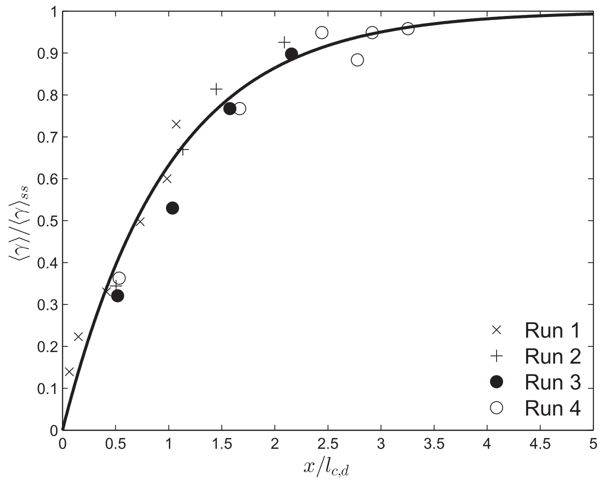

Fig. 1. Nondimensional particle activity $\langle\gamma\rangle/\langle\gamma\rangle_{ss}$ at several scaled distances $x/\ell_{c,d}$ in the experiments carried out by Jain [8] (Runs 1 and 2) and Bagnold [60] (Runs 3 and 4). The solid line represents the theoretical solution (15). The adaptation length $\ell_{c,d}$ was calibrated by fitting the dimensional solution $\langle\gamma\rangle(x)$ to each experimental series of Jain [8]. This yielded: $\ell_{c,d} = 17.67$ m, 6.35 m, 1.96 m, and 0.47 m for transport stage parameters $T = Sh/Sh_{cr} - 1 = 0.24$, 0.62, 1.68, and 16.6 from Run 1 to Run 4, respectively.

3.1. The adaptation length

The *adaptation length* (also called the saturation or relaxation length), denoted by $\ell_{c,d}$, is the characteristic distance that particles travel before reaching steady state after being entrained by the stream [59]; the sediment transport rate and particle activity also come close to their steady-state values $\bar{q}_{ss}$ and $\langle\gamma\rangle_{ss}$, respectively.

The parametric dependence of $\ell_{c,d}$ on flow variables remains unresolved in the numerical simulations dealing with transient flows and non-equilibrium sediment transport [15,17]. Using dimensional analysis arguments, Charru [59] found that the adaptation length for bedload transport is proportional to the particle velocity. More recently, Heyman et al. [25] suggested including particle diffusion in the definition of $\ell_{c,d}$. We shall see that our theory is consistent with [25] and retrieves Charru's [59] scaling in the absence of particle diffusion.

Heyman et al. [25] recently derived the expression of the adaptation length by calculating the steady-state solution to the mean advection–diffusion Eq. (7) for a prescribed uniform particle velocity $\bar{u}_s$ and the following boundary conditions:

$$\frac{\mathrm{d}}{\mathrm{d}x}(\bar{u}_s\langle\gamma\rangle) - \frac{\mathrm{d}^2}{\mathrm{d}x^2}(D_u\langle\gamma\rangle) = \lambda - \kappa\langle\gamma\rangle,$$
$$\langle\gamma\rangle = 0 \ \text{at}\ x = 0 \quad \text{and} \quad \frac{\mathrm{d}\langle\gamma\rangle}{\mathrm{d}x} = 0 \ \text{at}\ x \to \infty. \tag{14}$$

When $\bar{u}_s > 0$, solving Eq. (14) for $\langle\gamma\rangle$ (and assuming a constant sediment velocity $\bar{u}_s$) leads to:

$$\frac{\langle\gamma\rangle(x)}{\langle\gamma\rangle_{ss}} = 1 - e^{-x/\ell_{c,d}} \quad \text{with} \quad \ell_{c,d} = \frac{2\,D_u}{\bar{u}_s}\left[\sqrt{1 + 4\,\frac{D_u\,\kappa}{\bar{u}_s^2}} - 1\right]^{-1}. \tag{15}$$

When $\bar{u}_s = 0$, we get $\ell_{c,d} = \ell_d = \sqrt{D_u/\kappa}$. The adaptation length does not depend explicitly on the erosion rate λ, whereas the steady-state particle activity $\langle\gamma\rangle_{ss}$ [see Eq. (12)] is affected by λ. To leading order, $\ell_{c,d}$ is expected to reflect the balance between particle advection and deposition [59]. Indeed, the Taylor series expansion at $D_u = 0$ up to the fifth order,

$$\ell_{c,d} = \ell_c + \ell_d\left[\frac{\ell_d}{\ell_c} - \left(\frac{\ell_d}{\ell_c}\right)^3 + 2\left(\frac{\ell_d}{\ell_c}\right)^5 + O\left(\left(\frac{\ell_d}{\ell_c}\right)^7\right)\right], \quad \ell_c = \frac{\bar{u}_s}{\kappa}, \quad \ell_d = \sqrt{\frac{D_u}{\kappa}}, \tag{16}$$

shows that $\ell_{c,d} \approx \ell_c$ in the limit $\ell_d \to 0$, where ℓ_c is the adaptation length in the absence of particle diffusion (*i.e.*, $D_u = 0$), whereas ℓ_d is the adaptation length when advection is removed (*i.e.*, when $\bar{u}_s = 0$). In the absence of particle diffusion, our developments retrieve Charru's [59] scaling by setting $\ell_{c,d} = \ell_c = \bar{u}_s/\kappa$. How sediment diffusion affects the adaptation length (relative to particle advection) can be evaluated using the ratio $\ell_d/\ell_c = Pe^{-1} = (D_u\,\kappa/\bar{u}_s^2)^{1/2}$, which represents the inverse of the Péclet number [38]. For $Pe \gg 1$ (*i.e.*, $D_u\,\kappa \ll u_s^2$), particle advection is the predominant mechanism, whereas for $Pe \to 0$, sediment diffusion is the key process.

Fig. 1 shows the variation in $\langle\gamma\rangle$ with position. The labeled points correspond to Jain's and Bagnold's experimental data [8,60]. Neither Bagnold nor Jain measured the adaptation length. We therefore adjusted the theoretical scaled profiles $\langle\gamma\rangle(x)/\langle\gamma\rangle_{ss}$ on the experimental data. The adaptation lengths are $\ell_{c,d} = \{17.67,\ 6.35,\ 1.96,\ 0.47\}$ m, whereas the mass transport rates are $\varrho_s\bar{q}_{ss} = \{2.2,\ 19.0,\ 10.0,\ 148.0\}$ g (s m)$^{-1}$ for $T = \{0.24,\ 0.62,\ 1.68,\ 16.6\}$, where the transport stage parameter

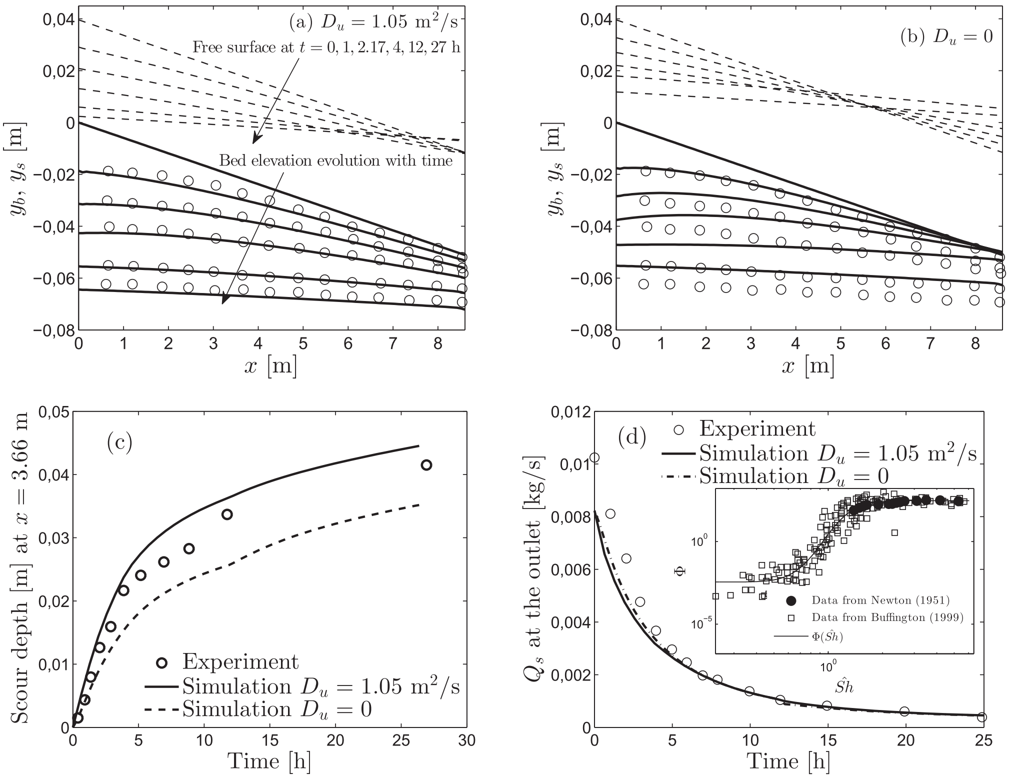

Fig. 2. Time variation of the bed (solid line) and free-surface (dashed line) elevations for (a) the diffusive and (b) non-diffusive cases for Run 3 of Newton [44]. (c) Local depth scour at $x = 3.66$ m. (d) Sediment transport rate at the flume outlet. The symbols (circles) correspond to the experimental measurements taken by Newton [44]. Similar to Fig. B.8, the inset in (d) represents the experimental values of Q_s in the plane $\{\Phi, \widehat{Sh}\}$ for $Sh_* = 0.04$ and $\varrho_s \bar{q}_{s*} = 10^{-5}$ kg/m s.

is defined as $T = Sh/Sh_{cr} - 1$, and ϱ_s denotes sediment density. The solid line is the exact solution (15). At the upstream boundary ($x = 0$), the particle activity vanishes owing to the prescribed Dirichlet boundary condition $\langle\gamma\rangle = 0$. Particles are carried by the stream ($\bar{u}_s > 0$), and so travel downwards (from left to right in Fig. 1). Particle activity increases monotonically with increasing x. Far from the inlet (*i.e.*, for $x \gg \ell_{c,d}$), the particle activity reaches its steady-state value $\langle\gamma\rangle = \langle\gamma\rangle_{ss}$. In practice, steady state is observed for $x \geq 3\,\ell_{c,d}$ because $\langle\gamma\rangle \geq 0.95\langle\gamma\rangle_{ss}$ according to the exact solution (15). The theoretical solution (15) closely matches the experimental data.

In the technical literature, the adaptation length $\ell_{c,d}$ is often associated with the bedform wavelength Λ [61]. In contrast to this common view, the theoretical solution (15) states that $\ell_{c,d}$ is independent of Λ. We refer the reader to Section 3.3 for further discussion about the selection mechanism for the wavelength Λ as a result of the coupling between the shallow-water balance Eqs. (1) and (2) and the sediment transport Eqs. (3) and (7): Λ is mostly controlled by the eddy diffusivity ν – introduced in the momentum balance Eq. (2) – of the water phase and particle diffusivity D_u of the sediment phase.

3.2. Newton's degradation experiment

Newton ran experiments on bedload transport in a flume including a 9.14 m long, 0.3 m wide, 0.6 m deep test reach [44]. A hopper filled with sand ($d = 0.69$ mm) fed the flume with sediment to ensure bed equilibrium along the flume. The bedload transport rate was maintained at equilibrium ($\bar{q}_s = \bar{q}_{ss}$) by recirculating sediment from the outlet to the inlet. Sediment supply was suddenly stopped to study bed degradation. The water discharge $Q = 0.0057$ m^3 s^{-1} was kept constant for the 27 h experiment duration. Newton monitored the bedload flux at the flume outlet, the bed and free surface elevations along the test reach at several time points (1, 2.17, 4, 12 and 27 h), and the evolution of the local scour depth at $x = 3.66$ m. The remaining data were used for testing the numerical results shown in Fig. 2. Initially, the bed was flat, inclined at the angle of 0.348° to the horizontal, the bed porosity was $\zeta_b = 0.396$, and the depth-averaged velocity was $V = 0.47$ m s^{-1}. The flow regime was subcritical with the Froude number $Fr = 0.75$ at $t = 0$. The data in the downstream reach of the flume ($x > 6$ m) were used for calibrating the model parameters under steady, uniform flow conditions, as described in Appendix C.

We adjusted the model parameter, $\lambda = 4.65 \times 10^{-5}\,(Sh - Sh_{cr})$ m s^{-1} with $Sh_{cr} = 0.044$, $\mu = 0$ and $\kappa = 0.245$ s^{-1}. The sediment velocity $\bar{u}_s$ and the friction factor f were evaluated from Eqs. (4) and (8) with a bed roughness factor $k_s = 4$ (calibrated using the initial conditions, as shown by El kadi Abderrezzak and Paquier [17]). In Eq. (2), the eddy viscosity

Table 1
Set of boundary conditions used in the numerical simulations. Physical and numerical (labeled with an asterisk) boundary conditions are imposed depending on the subcritical or supercritical flow regime, as explained in the main text. CVE means "characteristic variable extrapolation" method (see the text).

Channel degradation	
Inlet	Outlet
$\partial_x h = 0$ (*)	$h = h_{out}(t)$
$\bar{v}\,h = Q/B$, $\partial_x \bar{v} = 0$	$\partial_x\left(\bar{v}\,h + 2\sqrt{gh}\right) = 0$ (*)
$\partial_x\langle\gamma\rangle = 11.6\,\langle\gamma\rangle\exp(-0.8\,t/3600)$	$\langle\gamma\rangle = \langle\gamma\rangle_{ss}$
$\partial_x y_b = 0$	$\partial_x y_b = -f\,\bar{v}^2/8\,gh$
Anti-dune migration	
Inlet	Outlet
$\bar{h} = H$	CVE (*)
$\bar{v} = V$	CVE (*), $\partial_x \bar{v} = 0$
$\langle\gamma\rangle = \langle\gamma\rangle_{ss}$	$\partial_x\langle\gamma\rangle = 0$
$\partial_x y_b = 0$	$\partial_x y_b = -f\,\bar{v}^2/8\,gh$

was $\nu = \nu_t\, h\,\bar{v}\sqrt{f/8}$, with $\nu_t = 4$ [40]. In the numerical simulations, the length of the computational domain was 8.6 m, and the grid consisted of 100 cells. The time step in the numerical simulations was adjusted dynamically during the simulation process in order to satisfy the Courant–Friedrich–Lewy (CFL) stability condition [62]. With a CFL value of 0.25, the time step was close to 0.05 s.

The Péclet number $Pe = \beta V/\sqrt{D_u\,\kappa}$ was initially at its maximum ($Pe = 0.64$ at $t = 0$, with $\kappa = 0.245$ s^{-1}, $D_u = 1.05$ m^2 s^{-1}, and $\beta = 0.692$) when the bed slope was steepest. The adaptation length $\ell_{c,d} = 2.84$ m was initially larger than both the zero-diffusion length $\ell_c = 1.32$ m and the zero-advection length $\ell_d = 2.07$ m. Taking into account that $Pe \sim O(0.1)$ and $(\ell_{c,d} - \ell_c)/\ell_c \sim O(1)$, we expected the diffusive sediment transport rate $\bar{q}_{d,s}$ to be significant in the upper part of the flume (approximately for $x < 3\,\ell_{c,d}$). In other words, both particle advection and diffusion were expected to play a part in bedload transport.

Table 1 summarizes the boundary conditions employed in the numerical simulations. As the flow was subcritical during the experiment, we selected the following boundary conditions: (i) at the inlet, a constant water discharge Q, and (ii) at the outlet, a water depth $h_{out}(t)$ [see Fig. C.9(b)]. Two additional numerical boundary conditions (labeled with an asterisk in Table 1) were required in the first step of the fractional-step method, which solved the inviscid shallow water equations with source terms [63]. We followed the commonest approach by extrapolating the water depth from the inner computational domain to ghost cells at the flume inlet and by extrapolating the outgoing Riemann invariant at the flume outlet, as described by Blayo and Debreu [64]. The absence of local scour in Newton's experiments provided clear evidence that sediment was entrained from the sand reservoir into the test reach. Indeed, in the absence of sediment supply, degradation would have caused deep scour holes near the flume inlet [7]. Due to the lack of information on the experimental conditions, we performed an optimization process by varying the value of $\partial_x\langle\gamma\rangle$ that was imposed at the inlet. This procedure was repeated by varying the particle diffusivity from 10^{-4} m^2 s^{-1} to 100 m^2 s^{-1}. The optimum values for minimizing the root mean square error in the bed elevation y_b [see Fig. 2(a)] are given in Table 1 for $D_u = 1.05$ m^2 s^{-1}. Finally, we set the steady-state particle activity $\langle\gamma\rangle = \langle\gamma\rangle_{ss}$ at the flume outlet, which was realistic since the flume was much longer (~10 m) than the initial adaptation length ($\ell_{c,d} = 2.84$ m).

Fig. 2(a) shows that the simulated bed elevation (solid line) obtained with $D_u > 0$ is in good agreement with the experiments (empty circles) at all times. The Root Mean Square Error (RMSE) of the bed elevation ranged from 0.7 mm to 2.2 mm (see Table 2), and so was of the order of a grain size of $d = 0.69$ mm (*i.e.*, RMSE $\leq 3.2\,d$). The error was therefore negligibly small. The bed slope decreased progressively as degradation progressed until it reached a near steady state late in the experiment. The slope of the free surface (dashed line) remained nearly parallel to the bed. The flow depth increased with decreasing bed slope. In the absence of sediment diffusion [see Fig. 2(b)], a shallow scour hole developed next to the inlet when $t \leq 12$ h, but disappeared later in the experiment. A comparison between Figs. 2(a) and2(b) shows that when particle diffusivity was nonzero, the total sediment transport rate was higher under non-uniform flow conditions (degradation) than under uniform flow conditions. This is consistent with our analysis of ℓ_c and ℓ_d in the introduction of Section 3.2. As did El kadi Abderrezzak and Paquier [17] (see also [67]), we evaluated the model's performance using the Brier Skill Score:

$$\mathrm{BSS} = 1 - \frac{\sum_{i=1}^{M}\left(y_b^{exp}(x_i,t) - y_b^{num}(x_i,t)\right)^2}{\sum_{i=1}^{M}\left(y_b^{exp}(x_i,t) - y_b^{exp}(x_i,0)\right)^2}, \tag{17}$$

where superscripts *num* and *exp* refer to numerical result and experimental measurement, respectively, and M is the total number of experiments. The scores are reported in Table 2. Taking diffusion into account led to a BSS close to 1 throughout the numerical simulation. Such values were considered *excellent* by El kadi Abderrezzak and Paquier [17]. In the absence

Table 2
Root Mean Square Error (RMSE) and Brier Skill Score (BSS) defined by Eq. (17) for the simulation of the bed elevation y_b in Newton's experiment. Qualification ranges for BSS are [17,67]: excellent (1 – 0.8), good (0.8 – 0.6), fair (0.6 – 0.3), and poor (<0.3). For the sake of comparison with existing results, we also report BSS achieved by non-equilibrium sediment transport simulations run by El kadi Abderrezzak and Paquier [17], Davies et al. [65], and Zhang et al. [15].

Time (h)		1	2.17	4	12	27
Current model with diffusion	BSS	0.9124	0.9940	0.9967	0.9995	0.9969
	RMSE (m)	0.0020	0.0011	0.0013	0.0007	0.0022
Current model without diffusion	BSS	0.9542	0.8903	0.8880	0.9045	0.9678
	RMSE (m)	0.0014	0.0049	0.0075	0.0105	0.0072
El kadi Abderrezzak and Paquier [17]	BSS	0.81	0.96	0.97	0.94	0.98
	RMSE (m)	0.0029	0.0015	0.0014	0.0020	0.0018
CCHE1D [65,66]	BSS	0.8169	0.9872	0.9927	0.9947	0.9980
	RMSE (m)	0.0026	0.0015	0.0018	0.0023	0.0017
Zhang et al. [15]	BSS	0.9324	0.9628	0.9690	0.9996	0.9974
	RMSE (m)	0.0016	0.0029	0.0040	0.0009	0.0021

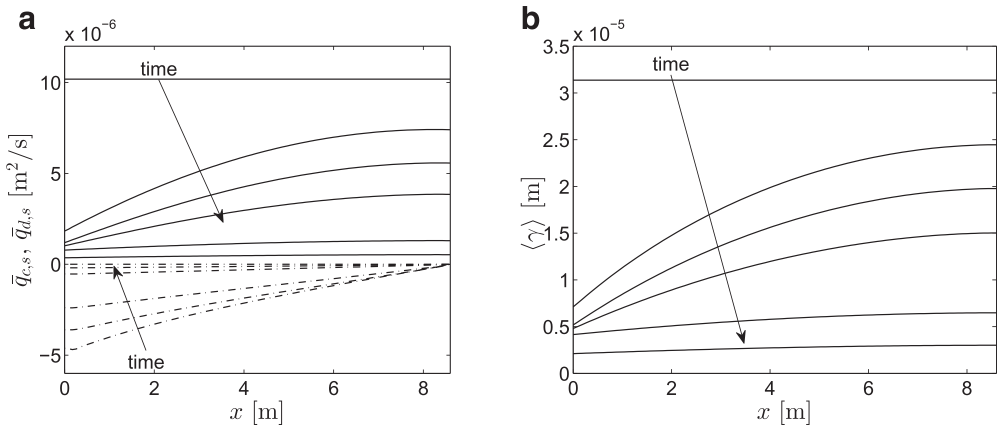

Fig. 3. (a) Advection and diffusion sediment transport rates ($\bar{q}_{c,s}$ and $\bar{q}_{d,s}$, respectively) in Newton's experiments at the same time points as Fig. 2(a). Panel (b) shows the streamwise profiles of the mean particle activity $\langle\gamma\rangle(x)$. Note that the particle activity tends to the steady-state value ($\langle\gamma\rangle = \langle\gamma\rangle_{ss}$) and that the diffusive sediment transport rate vanishes ($\bar{q}_{d,s} \approx 0$) near the end of the flume.

of diffusion, the BSS tended to 0.8 at $t = 4$ h (considered *good* by El kadi Abderrezzak and Paquier [17]). After long periods ($t = 27$ h), the agreement between the simulation and the experiment is better using $D_u = 1.05$ m^2 s^{-1} than $D_u = 0$. Fig. 2(c) shows the predicted scour depths at $x = 3.66$ m: for $D_u = 0$, these are too small, but for $D_u > 0$, they match the experimental values quite well. Fig. 2(d) shows the sediment transport rate at the outlet. As expected, the non-diffusive solution overlaps the diffusive solution because the flume is long enough for the flow to become uniform at the outlet. Both numerical solutions capture the experimental trend at this position. Next, we show that this can be better understood by taking a closer look at how convection and diffusion contribute to bedload transport.

Numerical simulations allow us to evaluate the relative importance of the convective and diffusive sediment transport rates. Fig. 3(a) shows these transport rates at the same time points as Fig. 2(a): the solid and dashed lines represent the convective sediment transport rate $\bar{q}_{c,s} = \bar{u}_s\langle\gamma\rangle$ and the diffusive rate $\bar{q}_{d,s} = -\partial_x D_u\langle\gamma\rangle$, respectively. The convective term $\bar{q}_{c,s}$ is positive as particles move downwards. The diffusive sediment transport rate $\bar{q}_{d,s}$ is negative because the particle activity $\langle\gamma\rangle$ increases monotonically from the flume inlet to the outlet; see Fig. 3(b). Since we have $\partial_x\bar{q}_{c,s} > 0$ and $\partial_x\bar{q}_{d,s} > 0$, both advection and diffusion contribute to eroding the bed. This explains why the water phase erodes more sediment when diffusion is taken into account. Furthermore, Fig. 2(a) and (b) show that bedload transport is out of equilibrium in the upper part of the flume, for $x < 3\,\ell_{c,d}$. This is reflected by the strength of the diffusive component of bedload transport and the variation of the ensemble-averaged particle activity $\langle\gamma\rangle$ with increasing x. Near the flume outlet, sediment transport reaches equilibrium, with $\langle\gamma\rangle \approx \langle\gamma\rangle_{ss}$ and $\bar{q}_{d,s} \approx 0$. This explains why, in Fig. 2(d), the sediment transport rate is independent of diffusivity.

3.3. The development of anti-dunes in the gravel bed stream

In gravel bed streams, initially planar beds may become unstable even under steady uniform flow conditions, and in that case, anti-dunes may develop. Here, we show that the SVE Eqs. (1)–(3) and (7) successfully reproduce anti-dune instability. Mathematically, within the framework of linear stability analysis, this is revealed by the existence of saddle points in the wavenumber space, which make the flow absolutely unstable. Furthermore, Eqs. (1)–(3) and (7) catch the most unstable

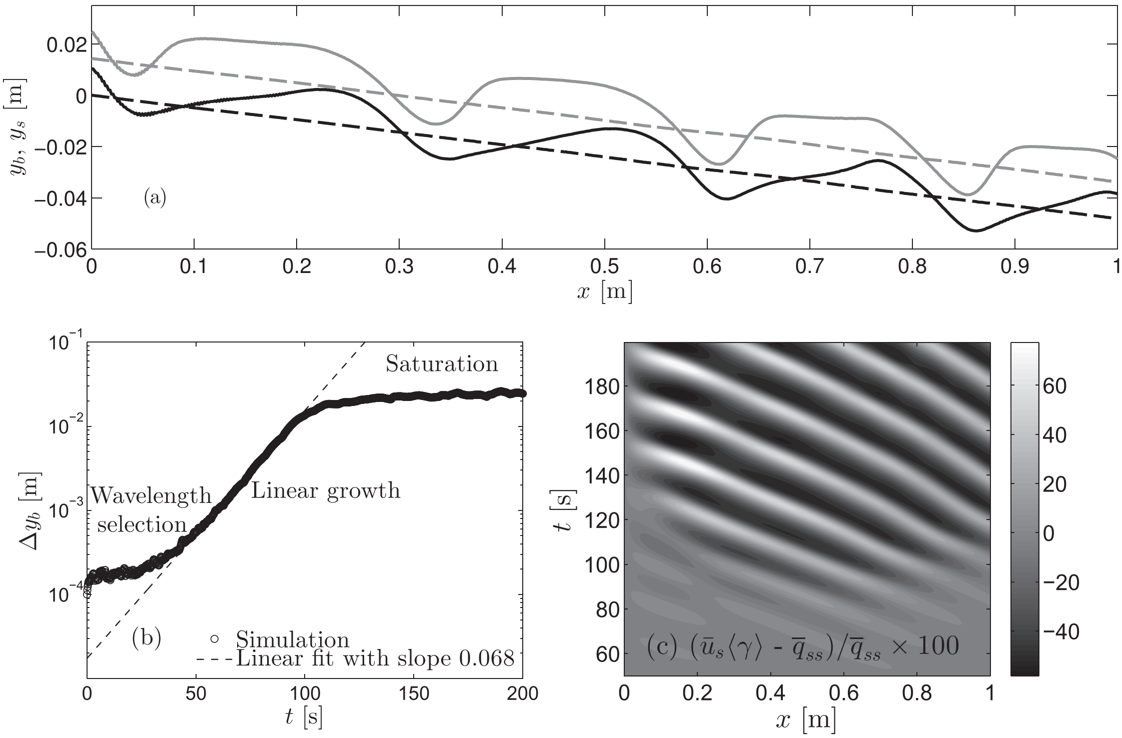

Fig. 4. (a) Snapshots of the bed and free-surface elevations together at $t = 0$ and at $t = 200$ s: dashed lines show the uniform base flow at $t = 0$; solid lines show the anti-dune train in the numerical simulation at $t = 200$ s. The gray and black lines correspond to the free surface and bed elevation, respectively. (b) Evolution of the maximum perturbation in the bed elevation. (c) Convection contribution to the bedload transport rate in the plane $\{x, t\}$ scaled by the uniform background flow's steady-state transport rate $\bar{q}_{ss}$.

wavelength. In the following, we first illustrate the development of upstream migrating anti-dunes in the simulations of shallow water flows over sloping erodible gravel beds. We then use spatiotemporal stability analysis [68,69] to show the absolute nature of the instability. This allows us to predict the most unstable wavelength theoretically. In contrast, when the Saint-Venant Eqs. (1) and (2) are coupled with the standard Exner equation, the bed is unconditionally stable for $Fr < 2$ [70] and, consequently, the anti-dune diagram cannot be computed.

The flow parameters used in the simulations corresponded to the dimensionless numbers $Fr = 1.2$ and $\delta^2 = 0.4$, which came close to the experimental conditions imposed by Cao [45], Bathurst et al. [46], Recking et al. [47], and Mettra [48]. The length and width of the channel were similar to those used in Mettra's [48] experiments: $L = 1.5$ m and $B = 8$ cm. Without a loss of generality, we set the critical Shields number to $Sh_{cr} = 0.03$ (this corresponds to fine/medium gravel [71]), whereas the Darcy–Weisbach friction factor f was evaluated from Eq. (4) with $k_s = 1$. The slope angle, Shields number, and sediment-to-water velocity ratio associated with this set of values were computed from Eqs. (10) and (11), which yielded $\theta = 2.75^\circ$, $Sh = 0.073$ (*i.e.*, we had $Sh/Sh_{cr} > 2$), and $\beta = 1$ under uniform flow conditions. Other model parameters were kept constant during the numerical simulation: $d = 5.74$ mm, $\mu = 0$, $\kappa = 5.31$ s^{-1}, $\zeta_b = 0.36$, and $D_u = 0.1$ m^2 s^{-1}. Substituting these values into Eqs. (B.2), (15) and (16), we obtained the steady-state bedload transport rate $\bar{q}_{ss} = 1.07 \times 10^{-4}$ m^2 s^{-1} (86.49 part. s^{-1}), the adaptation lengths $\ell_{c,d} = 18.6$ cm, $\ell_c = 8.5$ cm, and $\ell_d = 13.7$ cm, and the Péclet number $Pe = 0.617$ for the uniform base flow $h = 1.43$ cm and $\bar{v} = 0.45$ m s^{-1}. The steady-state bedload transport rate $\bar{q}_{ss}$ was used to establish the importance of sediment advection relative to diffusion in the presence of anti-dunes under unsteady non-uniform flow conditions.

As in the previous simulations, the eddy viscosity was approximated by $\nu \approx \nu_t\, h\, \bar{v}\sqrt{f/8}$ with $\nu_t = 10$. The computational domain $0 \le x \le 1.5$ m was divided into 1000 cells. As the flow was supercritical at the inlet at all times during the numerical simulation, we imposed the boundary conditions summarized in Table 1. At the inlet, the water depth and the flow depth-averaged velocity were set to $H = 1.43$ cm and $V = 45$ cm s^{-1}, respectively, and the particle activity took its steady-state value. At the outlet, the *characteristic variable extrapolation* method (CVE) was employed for computing the three Riemann invariants that travel outwards. In addition, a fairly good *sponge* layer was added in the outlet reach $x > 1$ m to ensure absorbing boundary conditions [72]. The initial conditions used in our computations were $h = H$, $\bar{v} = V$, $\langle\gamma\rangle = \langle\gamma\rangle_{ss}$, and $y_b = -x \tan\theta + \epsilon(x)$ where $\epsilon(x)$ is a random perturbation with amplitude 10^{-4} m. Below, we report on the results in the reach $0 \le x \le 1$ m, which is not affected by the sponge layer.

Fig. 4(a) shows the initial condition for the bed (black dashed line) and free-surface (gray dashed line) elevations. The initial perturbation introduced in the bed elevation cannot be observed because of its small amplitude. After a first

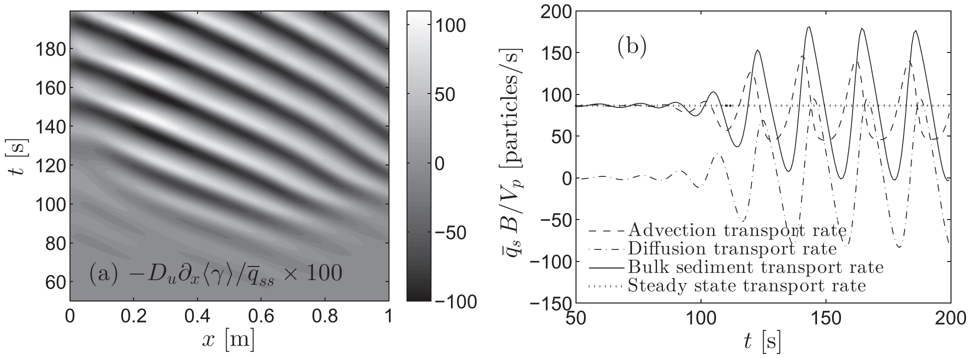

Fig. 5. (a) Diffusion contribution to the sediment transport rate in the plane $\{x, t\}$ scaled by the uniform background flow's steady-state value $\bar{q}_{ss}$. (b) Comparison between the diffusive (dotted-dashed line), convective (dashed line), and total (solid line) sediment transport rates with respect to the steady-state sediment transport $\bar{q}_{ss}$ (dotted line) at $x = 24$ cm.

stage in which the numerical solution self-selects a well-defined wavelength (for $t \le 50$ s), the bed perturbation grows as $\Delta y_b(t) = \max(|y_b(x,t) - y_b(x,0)|) = \exp(0.068\,t)$, until time $t \approx 100$ s when the maximum amplitude of the bed perturbation saturates, as shown in Fig. 4(b). The numerical solution at later time points (solid lines) exhibits a train of anti-dunes with amplitudes as high as the initial water depth and a similar wavelength $0.2 \le \Lambda \le 0.3$ m. The wavelength is slightly coarser upstream than downstream, which could be attributed to a nonlinear coarsening mechanism during the growth and propagation of anti-dunes from the reach outlet to the inlet. The water surface y_s and the bed elevation y_b are no longer planar as a result of bedform development. The free surface curvature is marked above the anti-dune's lee side whereas above the stoss side, the free surface remains nearly parallel to the initial bed. Obviously, the flow velocity $\bar{v}$ and Shields number are non-uniform in the perturbed state, which induces spatiotemporal variations in the sediment transport rate $\bar{q}_s$.

The fluctuations in the sediment transport rate can be seen in Figs. 4(c) and 5(a), where the convective and diffusive rates, $\bar{q}_{c,s}$ and $\bar{q}_{d,s}$, have been compared to the steady-state sediment transport rate $\bar{q}_{ss}$. The fluctuations in the convective transport rate reach $\pm$ 60% of its steady-state value. The diffusive transport rate is even higher – approximately $-\bar{q}_{ss} \le \bar{q}_{d,s} \le 1.1\,\bar{q}_{ss}$. The sediment transport rate's maximum deviation from its steady-state value is reached at $x \approx 0.24$ m. A detail from the evolution of each sediment transport component is shown in Fig. 5(b). The bedload transport rate exhibited large temporal fluctuations relative to its the mean value $\bar{q}_{ss}$ for $t \ge 150$ s, after the first transient stage. Note that the diffusive transport rate (dotted-dashed line) is as high as the steady-state value (dotted line), which highlights the importance of particle diffusion in sediment transport. There was a time lag in the convective and diffusive transport rate fluctuations, but they did not counterbalance each other. Hence, the total sediment transport also exhibited large fluctuations with a well-defined frequency. Overall, the diffusive component is expected to be dominant in any shallow-water flow developing bedforms, such as dunes and anti-dunes, when their heights are comparable to the flow depth under uniform flow conditions. Otherwise, as happens for ripples and dunes in deep water, when the free surface does not interact with the bedforms, flow is uniform; consequently, diffusive transport dies out or, at least, becomes negligible compared to advective transport.

The spatial wavelength (and the temporal frequency) observed numerically in the nonlinear cycle at later time points ($t \ge 150$ s) can be predicted using a spatiotemporal linear stability analysis. Here we follow the procedure presented in an earlier publication [40]: (i) we define the dimensionless variables $z = y_b/H$, $\phi = \langle\gamma\rangle/\langle\gamma\rangle_{ss}$, $\eta = h/H$, $u = \bar{v}/V$, $\hat{x} = x\tan\theta/H$, and $\hat{t} = tV\tan\theta/H$; (ii) we linearize the dimensionless SVE equations around a uniform base flow by setting $(z, \phi, \eta, u) = (-\hat{x}, 1, 1, 1) + \epsilon\,(z', \phi', \eta', u')$ and retain only the terms of order $O(\epsilon)$, which leads to the linear perturbation equation with an exponential solution (see Appendix D); and (iii) we determine the saddle and cusp points of the eigenvalue problem. The first and second steps of this procedure are detailed in Sections 3.1 and 3.2 in [40], and thus are not repeated here. The focus is on determining the saddle points.

Substituting the set of values used for the numerical simulation of anti-dunes in (D.2), we get $k_e = 0.0864$, $k_d = 4.52$, $u_* = 0.64$, $\mathcal{V} = 0.125$, $\mathcal{D} = 0.745$, and $\beta = 1$. The dimensionless wavenumber associated with the natural wavelength growing in the simulation ($\Lambda = 0.2$ m that grows spontaneously in the simulation) is $k = 2\pi H/(\Lambda\tan\theta) = 9.36$ at the flume's downstream reach. Its corresponding temporal frequency in the linear stability analysis is obtained from the solution to the dispersion relation $\mathbb{D}(k,\omega) \equiv |\bar{\bar{A}}| = 0$ [see Eq. (D.1)], which yields $\omega_i = 0.044$ ($\omega_i V\tan\theta/H = 0.0674$ s^{-1}). This value is in close agreement with the numerical growth rate 0.068 s^{-1} obtained in Fig. 4(a). Furthermore, the dispersion relation is instrumental to finding the saddle points, whose existence explains why a well-defined wavelength emerges in the numerical simulations [68,69].

In our model, for the current set of dimensionless parameters, multiple saddle points exist at $k = -i\,1.197$ [$\omega = i\,0.0112$, see Fig. 6(a)] and $k = 6.4 + i0.6$ [$\omega = 0.18 + i\,0.054$, see Fig. 6(b)], with branches k^+ and k^- originating from distinct halves of the k-plane. The self-selected wavenumber is defined as the point of intersection between the path connecting two saddle points and the real axis $k_i = 0$. This point corresponds to the maximum growth rate in the temporal stability analysis. Here

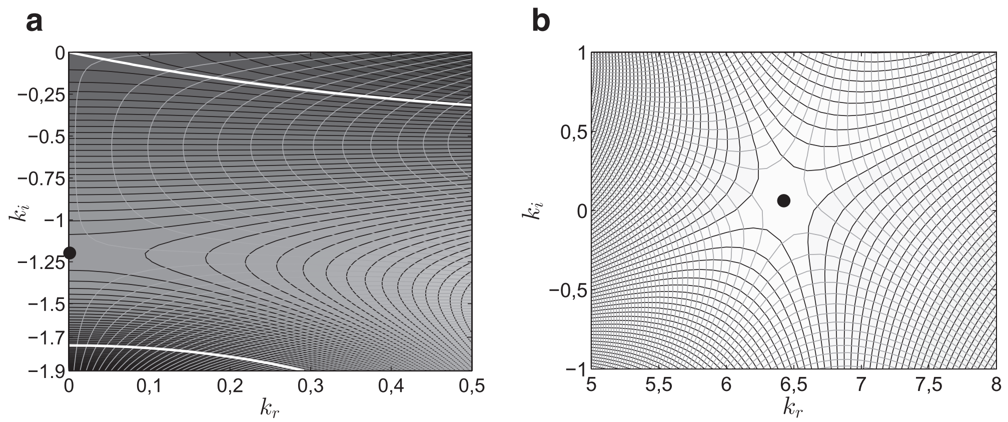

Fig. 6. The black dots show the location k_0 pinch points in the complex wavenumber plane $\{k_r, k_i\}$ using Briggs' method (isocontours of $\omega_r(k)$ and $\omega_i(k)$) for the parameter values in the numerical simulation of anti-dunes. The saddle points $k = -i\,1.197$ (a) and $k = 6.4 + i0.6$ (b) are pinched between branches k^+ (half-plane $k_i > 0$) and k^- (half-plane $k_i < 0$) issuing from distinct halves of the k-plane. Spatial branches $k^{\pm}(\omega)$ with $\omega_i = 0$ are colored in white.

we find $k = 6.24$ and $\omega = 0.18 + i\,0.0536$. The point of intersection lies close to the saddle point in Fig. 6(b) because the latter approaches the real axis. Consequently, the second saddle point that lies on the imaginary axis controls bed instability [see Fig. 6(a)]. The dimensional wavenumber in the numerical simulation satisfies $6.24 \le 2\pi H/\Lambda \tan\theta \le 9.3$, and this is consistent with the theoretical result $k = 6.24$. There is therefore a close agreement between linear stability theory and numerical simulations.

4. Discussion. Comparison with existing approaches to bedload transport

Different approaches to bedload transport have been used in numerical models: incorporation of an empirical bedload transport equation $\bar{q}_{ss}(Sh)$ into the standard Exner Eq. (18), the flux relaxation equation for quasi-steady, non-diffusive sediment transport [7,8], and non-equilibrium bedload transport equations [1] (also referred to as unsteady flux relaxation equations). We show that all of these approaches are special examples of the SVE Eqs. (1)–(7).

The bedload transport rate $\bar{q}_s$ reaches its steady-state value $\bar{q}_{ss}(Sh)$ under steady, uniform flow conditions, *i.e.*, when $\partial_x \bar{q}_s = \partial_t\langle\gamma\rangle = 0$. Thus, $E = D$ according to the mass balance condition (7), and there is no aggradation or degradation of the bed, *i.e.*, $\partial_t y_b = 0$. The equilibrium transport approach assumes that the relation $\bar{q}_s = \bar{q}_{ss}(Sh)$ also holds under non-uniform flow conditions. The Exner Eq. (3) is cast in the following form:

$$(1-\zeta_b)\frac{\partial y_b}{\partial t} + \frac{\partial \bar{q}_{ss}}{\partial x} = 0\,. \tag{18}$$

Formally, this approximation is valid under slowly varying flow conditions (when $\partial_t\langle\gamma\rangle \ll \lambda$) and in the absence of a strong gradient in the sediment transport rate ($\partial_x \bar{q}_{ss} \ll \lambda$).

The flux relaxation equation holds for quasi-steady, non-diffusive sediment transport [7,8]. By setting $D_u = 0$ (*i.e.*, $\bar{q}_s = \bar{u}_s\langle\gamma\rangle$), neglecting the temporal variation $\partial_t\langle\gamma\rangle$, and substituting Eqs. (7) and (9) into Eq. (3), we end up with the standard version of the Exner equation [73]:

$$(1-\zeta_b)\frac{\partial y_b}{\partial t} + \frac{\partial \bar{q}_s}{\partial x} = 0. \tag{19}$$

In this case, the bedload transport rate $\bar{q}_s$ is derived from Eqs. (7) and (9). We thus obtain the *flux relaxation equation*:

$$\frac{\partial}{\partial x}(\beta\,\bar{v}\,\langle\gamma\rangle) = \lambda - \kappa\,\langle\gamma\rangle \quad \text{or} \quad \frac{\partial \bar{q}_s}{\partial x} = -\frac{1}{\ell_c}(\bar{q}_s - \bar{q}_{ss})\,, \tag{20}$$

where the adaptation length is $\ell_c = \bar{u}_s/\kappa$.

There is a mathematical similarity between the non-equilibrium bedload transport equations [1] and the ensemble-averaged SVE Eqs. (1)–(3) and (7). Indeed, by neglecting sediment diffusion (*i.e.*, $D_u = 0$) and using the definition of the local bedload transport equation $\bar{q}_s = \bar{u}_s\langle\gamma\rangle$, we can recast Eqs. (3) and (7) in the following forms:

$$(1-\zeta_b)\frac{\partial y_b}{\partial t} = -\frac{1}{\ell_c}(\bar{q}_{ss} - \bar{q}_s)\,, \tag{21}$$

$$\frac{\partial}{\partial t}\left(\frac{\bar{q}_s}{\bar{u}_s}\right) + \frac{\partial \bar{q}_s}{\partial x} = -\frac{1}{\ell_c}(\bar{q}_s - \bar{q}_{ss})\,. \tag{22}$$

In the limiting case where $|\partial_x \bar{q}_s| \ll \lambda$, the leading-order solution to the flux relaxation Eq. (20) is $\langle\gamma\rangle = \langle\gamma\rangle_{ss}$ or $\bar{q}_s = \bar{q}_{ss}$, which shows that our model is consistent with the Exner equation based on the algebraic bedload transport equation

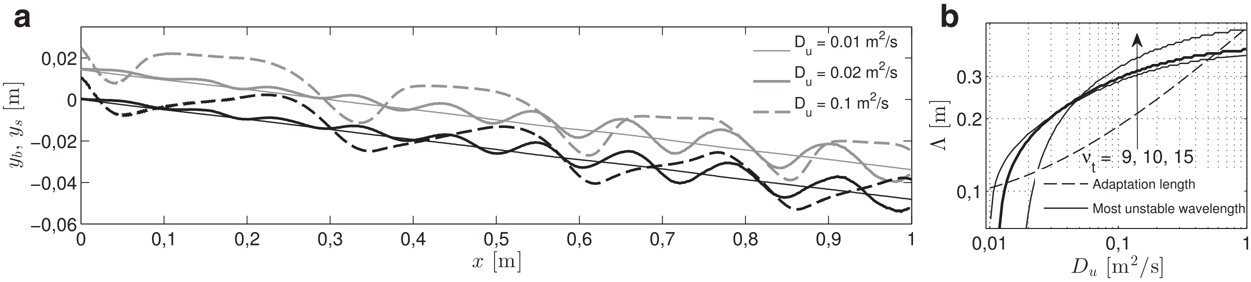

Fig. 7. Sensitivity analysis of the anti-dune wavelength as a function of the particle diffusivity D_u and the dimensionless eddy viscosity ν_t (the rest of the parameters are constant, see Section 3.3). (a) Numerical results at $t = 200$ s for $D_u = 0.01$ m^2 s^{-1}, 0.02 m^2 s^{-1}, and 0.1 m^2 s^{-1}. (b) The most unstable wavelength in the temporal stability analysis (continuous line). The dashed line shows the adaptation length $\ell_{c,d}$ (15). The thicker line corresponds to the value $\nu_t = 10$ used in the numerical simulations.

$\bar{q}_{ss}$ (18). By defining the adaptation length as $\ell_c = \bar{u}_s/\kappa$, we also retrieve the flux relaxation equation obtained by Charru [59]. It is worth mentioning that El kadi Abderrezzak and Paquier [17] successfully computed several problems of practical relevance using Eqs. (19) and (20), and Li and Qi [74] built analytical solutions related to bed degradation under slowly varying flow conditions by using a constant adaptation length ℓ_c. These examples provide evidence that our variant of the Exner Eq. (20) (or Eq. (7)) performs better than the classic Exner Eq. (18). Note also that Eqs. (21) and (22) are similar to the non-equilibrium bedload equations [1,15]. Some authors prefer to express them in terms of an equivalent depth-averaged volumetric concentration of sediment [12,75], whereas others keep the mean particle activity $\langle\gamma\rangle$ (instead of $\bar{q}_s$) as the unknown to be determined [9,76]. This shows that most (if not all) sediment transport equations ignore particle diffusion in the calculation of the mean particle activity or mean sediment transport rate.

Each approach cited above performs differently depending on the test scenario. For the degradation of a sloping bed presented in Section 3.2, Table 2 shows the BSS and the RMSE scores obtained by numerical models based on the quasi-steady flux relaxation equation [17] and the non-equilibrium flux relaxation equation [15,65] at five different time points ($t = 1$, 2.17, 4, 12, and 27 h). According to the BSS qualification suggested by Davies et al. [67], all three approaches achieve excellent marks. There are, however, quantitative differences that allow us to establish that the most complex model is also the most accurate. The BSS is at all times larger than 0.9 for the SVE equations with diffusion and for the zero-diffusion non-equilibrium model by Zhang et al. [15]. Nearly perfect marks (BSS > 0.98) at $t > 1$ h are achieved with the diffusive SVE equations and the non-equilibrium model implemented in the CCHE1D software [65,66]. Our model (BSS = 0.91) outperforms CCHE1D (BSS = 0.81) at $t = 1$ h. In contrast, assuming steadiness in Eq. (20) leads to a slight error in the numerical outputs, which is reflected by lower BSS and RMSE scores. A comparison with the equilibrium transport theory (18) was not possible because existing solutions (*e.g.*, see [77]) correspond to experimental conditions that differ from those studied in this paper.

A more sensitive test scenario is the numerical simulation of anti-dune migration on a sloping gravel bed (see Section 3.3), and so it can be considered an excellent benchmark for approaches to bedload transport. The key parameter is particle diffusivity, because: (i) it increases the order of the characteristic polynomial to $O(k^2)$ [see Eq. (D.1)] when $D_u > 0$; (ii) it controls the existence of mathematical solutions to the Briggs–Bers condition; and (iii) it causes absolute instability (or wavelength selection). This last point is corroborated by the nonlinear numerical simulations shown in Fig. 7(a) for the same parameters as in Fig. 4 with $D_u = 0.01$ m^2 s^{-1} (thin solid line) and 0.02 m^2 s^{-1} (thick solid line). For the sake of comparison, the solution for $D_u = 0.1$ m^2 s^{-1} (dashed line) is also shown. The anti-dune wavelength is shorter as D_u decreases from 0.1 m^2 s^{-1} to 0.02 m^2 s^{-1}, which is consistent with the linear stability results. The most unstable wavelength Λ in the temporal stability analysis increases monotonously as particle diffusivity increases [see thick solid line in Fig. 7(b)]. At low values of D_u, Λ sharply decreases, and bedform instabilities develop only for $D_u > 0.0114$ m^2 s^{-1}. This explains why the bed remains flat in the numerical simulation using $D_u = 0.01$ m^2 s^{-1}, consistent with the linear stability results. It also explains why the SVE equations based on zero-diffusion, non-equilibrium (or equilibrium) bedload transport theory alter bedform development. Similar results are obtained when the dimensionless eddy viscosity ν_t is raised from 9 to 15. Fig. 7(b) shows the analytical solution (15) for the adaptation length $\ell_{c,d}$ (dashed line). Both the adaptation length and the bedform wavelength are independent of each other because they represent distinct physical processes and thus are solutions to different mathematical problems.

Our ensemble-averaged SVE equations have limitations that arise from our working assumptions. Two limiting cases are worthy of discussion. For Shields numbers close to the threshold of incipient motion, the particle activity γ exhibits wide fluctuations, which may be much larger than the mean value $\langle\gamma\rangle$ [39,78]. This has prompted the development of statistical tools for describing sediment transport. In our approach, the deterministic advection–diffusion Eq. (7) can be replaced with the stochastic Langevin Eq. (A.1). Recall that we ended up with Eq. (7) by taking the ensemble average of the Langevin Eq. (A.1). In a recent paper [40], we showed that coupling the stochastic Langevin Eq. (A.1) and the deterministic Saint-Venant–Exner Eqs. (1)–(3) was straightforward, from a numerical point of view, regardless of the order of accuracy of the scheme adopted in the finite volume method (first-order upwind, second-order TVD, or fifth-order WENO scheme). At low Shields numbers, sandy beds also develop ripples and dunes that migrate downstream. Preliminary results (which will be reported in a forthcoming paper) indicate that a phase lag in the friction factor f is needed to allow for downstream migrating bedforms when we use the SVE equations, and this is consistent with Kennedy's [79] theory. At high Shields numbers, however, bedforms are washed out by the flow and the transition to an upper-stage plane bed, sheet flow, and suspended sediment transport may occur. More elaborate models are then needed for modeling bedload transport. Typical examples include models based on mixture theory and the two-phase flow equations presented in [10–12,14,15]. Note that the birth–death Markov process theory that underpins the derivation of the Langevin Eq. (A.1) is not consistent when multiple events occur at the same time [39,52], and so we expect that at larger Shields numbers, the parameterization we used in the SVE Eqs. (1)–(3) and (7) no longer holds.

5. Concluding remarks

In this article, we investigated the problem of bedload transport in shallow water flows over erodible beds by using the ensemble-averaged version, (1)–(3) and (7), of the stochastic Saint-Venant–Exner equations presented in an earlier publication [40]. The bulk sediment transport rate $\bar{q}_s = \bar{q}_{s,c} + \bar{q}_{s,d}$ defined by Eq. (9) is split into the advective transport rate reflecting the driving action of water ($\bar{q}_{s,c} = \bar{u}_s\langle\gamma\rangle = \beta\bar{v}\langle\gamma\rangle$) and the diffusive rate due to the spatial gradient of the mean particle activity ($\bar{q}_{s,d} = -D_u\partial_x\langle\gamma\rangle$) [37]. However, in contrast to classic theories, we take diffusion into account. The diffusive term $-D_u\partial_{xx}\langle\gamma\rangle$ in Eq. (7) results from the ensemble average of the stochastic Langevin Eq. (A.1) [38].

The relative importance of the diffusive and advective transport rates was studied numerically by considering two test scenarios: (i) the degradation of a sloping bed and (ii) the non-uniform flow that results from the development and migration of anti-dunes in gravel bed streams on a steep slope. In test scenario (i), the diffusive transport rate was dominant in the upstream reach of the flume in the early stage of the scouring process; it died out in the downstream reach of the channel where the flow was almost uniform. There was an excellent agreement between the numerical results and experimental measurements taken by Newton [44] (see Fig. 2). This encouraging result substantiated our approach and its numerical implementation. Test scenario (ii) provided evidence that the ensemble-averaged SVE Eqs. (3)–(7) can simulate upstream migrating bedforms and predict the anti-dune wavelengths. Our numerical results were qualitatively consistent with the phenomenological description in the seminal experimental work done by Kennedy [80] (pp. 104–114), who stated that "it was impossible to prevent large disturbances at the inlet (...) the disturbance at the downstream end of the flume caused a train of waves to form." Indeed, we observed wide fluctuations in bed elevation and the sediment transport rate next to the flume inlet as anti-dunes migrated from the outlet to the inlet [see Figs. 4–5].

The strong analogy that exists between the ensemble-averaged SVE Eqs. (3)–(7) and the non-equilibrium sediment transport Eqs. (21) and (22) (also referred to as unsteady flux relaxation equations) was emphasized in Section 4. We firmly believe that embedding diffusion into deterministic non-equilibrium sediment transport equations is key to improving the predictive capability of existing numerical models. On the whole, we found that the advective and diffusive transport rates had the same order of magnitude at certain stages of bedload transport (typically under non-uniform flow conditions). Entrainment, deposition, convection, and diffusion mechanisms compete with each other depending on the value of the Péclet number $Pe = l_c/l_d = (\bar{u}_s^2/D_u\kappa)^{1/2}$. The prevalent sediment transport mechanism is convection when $Pe \gg 1$, a limiting state in which the adaptation length $l_{c,d}$ tends to $l_c = \bar{u}_s/\kappa$; it is diffusion when $Pe \ll 1$ and $l_{c,d} \approx l_d = \sqrt{D_u/\kappa}$.

To conclude, we would again like to highlight that the versatile numerical framework described in this paper – and in [40] – makes it possible to use either deterministic or stochastic formulations of bedload transport within the same numerical framework.

Acknowledgments

Patricio Bohorquez acknowledges the financial support from the Spanish Ministry of Economy and Competitiveness through research project SEDRETO (CGL2015-70736-R), the Caja Rural Provincial de Jaén, the University of Jaén (projects # UJA2014/07/04 and UJA2013/08/21) and CEACTierra (project # 2013/00065/001). Christophe Ancey was supported by two Swiss National Science Foundation Grants, nos. 200021–129538 and 200021–160083 (projects called "The Stochastic Torrent: stochastic model for bedload transport on steep slope").

Appendix A. Derivation of the advection–diffusion equation

In this appendix, we explain how the advection–diffusion Eq. (7) was derived. This equation is the ensemble average of a stochastic partial differential equation with a colored noise term; it was derived in [38,39]:

$$\frac{\partial b}{\partial t} + \frac{\partial}{\partial x}(\bar{u}_s b) - \frac{\partial^2}{\partial x^2}(D_u b) = E' - D' + \sqrt{2\mu b}\,\xi_b\,, \tag{A.1}$$

where b is the Poisson density [part. m^{-1}], γ is the particle activity [m], μ [s^{-1}] is an entrainment parameter called the *collective entrainment coefficient*, and ξ_b [(m s)$^{-1/2}$] is a Gaussian noise term. We also introduced the entrainment and deposition rates per unit streambed area, E' [part. s $^{-1}$m^{-1}] and D' [part. s^{-1} m^{-1}], respectively. The stochastic and deterministic entrainment and deposition rates are related by $\langle E'\rangle = EB/V_p$ and $\langle D'\rangle = DB/V_p$, where $V_p = \pi d^3/6$ is the typical particle volume. Eq. (A.1) is a stochastic (Langevin) partial differential equation [38,39,52]. Itô's convention is used for defining and interpreting stochastic integration [81].

The stochastic model was built on a birth-death Markov process describing the number N of moving particles within a set window of length Δx and width B [52]. This number varies when particles enter the window, leave it, are entrained from the bed, or are deposited on the bed. As events occur randomly, N is a discrete random variable. Jump Markov process theory leads to a stochastic differential equation (the forward Kolmogorov equation) describing the evolution of the probability $P(N)$ of observing N [38,52]. Furthermore, we assume that particles are all the same (with the same size and weight). As we work with continuum equations, it is more convenient to handle a continuous random variable instead of the discrete variable N. To that end, we introduce the particle activity:

$$\gamma = \frac{V_p}{B\Delta x} N . \tag{A.2}$$

The stumbling block is that when taking the continuum limit $\Delta x \to 0$, one cannot transform the forward Kolmogorov equation into a stochastic partial differential equation for γ (because the Kolomogov equation is a delay equation of $P(N)$). There are a number of different strategies available to overcome this hurdle [38,39,53]. Here, we use an exact analytical technique called the *Poisson representation* in order to pass from the discrete variable N to the continuous random variable b [81]. This representation can be thought of as a Laplace or Fourier transform, and it performs remarkably well for delay equations. Taking the Poisson representation of the forward Kolmogorov equation governing N leads to the evolution Eq. (A.1) for b. Under special conditions, (*e.g.*, a homogeneous steady state), this equation can be solved exactly, however on most occasions it has to be solved numerically. One drawback of this is that there is no formal inverse Poisson representation that would enable us to pass from b to N. Nevertheless, an interesting feature of the Poisson representation is that one can relate the first-order moments of b and N, therefore, Eq. (7) is derived by taking the ensemble average of Eq. (A.1) and the continuum limit $\Delta x \to 0$ [39].

We now comment on the physical meaning of Eq. (A.1). The Poisson density b satisfies a stochastic advection–diffusion equation including a source term and a non-negative colored term. When the collective entrainment coefficient μ is zero, Eq. (A.1) becomes deterministic. This means that the number of moving particles N behaves like a nonhomogeneous Poisson process, with small fluctuations around the mean (large fluctuations are rare events). When $\mu > 0$, the behavior of N is non-Poissonian, with large and frequent fluctuations of N around the mean [39,52]. It can then be deduced that the collective entrainment coefficient μ plays a key role in the fluctuation dynamics. Eq. (A.1) describes how fluctuations of γ are generated by the source terms, advected by the particles, and attenuated by diffusion.

Appendix B. A new empirical bedload transport equation

In this appendix, we derive an empirical equation for steady-state particle activity $\langle\gamma\rangle_{ss}$. This empirical equation sets the value of the λ/κ ratio [see Eq. (12)] and can thus be used to calibrate the model parameters:

$$\frac{\lambda}{\kappa} = \langle\gamma\rangle_{ss} = \frac{\bar{q}_{ss}(Sh)}{\bar{u}_s} = \frac{\bar{q}_{ss}(Sh)}{\beta\,\bar{v}} . \tag{B.1}$$

The idea underpinning this derivation is that at sufficiently high Shields numbers, the sediment transport rate can be estimated using empirical algebraic bedload transport equations $\bar{q}_{ss}(Sh)$, such as the equation proposed by Fernandez Luque and van Beek [56]:

$$\bar{q}_{ss} = \langle\gamma\rangle_{ss}\,\bar{u}_s \quad \text{with} \quad \langle\gamma\rangle_{ss} = \frac{\lambda}{\kappa} = \frac{c_e V_p}{c_d\, d^2}\,(Sh - Sh_{cr}) , \quad \bar{u}_s = \beta\,\bar{v} , \tag{B.2}$$

where $c_e/c_d = 1.75$ [56,76] and the sediment-to-water velocity function $\beta \le 1$ is given by Eq. (8) or any combination of parameters that represent the particle size and the turbulent boundary layer characteristics at the bottom, *e.g.*, see [61]. The steady-state particle activity $\langle\gamma\rangle_{ss}$ can be deduced because, under steady, uniform flow conditions, the particle activity and sediment transport rate are linearly related [see Eq. (9)].

This approach is, however, not free of bias if one applies it without caution. Among other things, algebraic bedload transport equations $\bar{q}_{ss}(Sh)$ assume the existence of a constant critical Shields number Sh_{cr} below which there is no sediment transport, and they have been obtained by adjusting a power-law function $\bar{q}_{ss}(Sh) \propto (Sh - Sh_{cr})^n$ (with n an exponent close to 3/2) to experimental data at sufficiently high Shields numbers. As Sh_{cr} is notoriously difficult to define and measure [71], and the algebraic equations are usually adjusted to data satisfying $Sh > 2Sh_{cr}$, these equations are inaccurate in the limit $Sh \to 0$. This difficulty can be overcome by applying a corrective function that connects the low and high Shields number domains.

Buffington [71] studied bedload transport at low Shields numbers and showed that the sediment transport rate varies as $Sh^{17.5}$ in the limit $Sh \to 0$, whereas at large Shields numbers, an empirical bedload transport equation, such as Eq. (B.2), provides the scaling $\bar{q}_{ss} \propto Sh^{3/2}$ (since $\langle\gamma\rangle_{ss} \propto Sh$ and $\bar{u}_s \propto Sh^{1/2}$). We fitted a nonlinear function $\bar{q}_{ss} = F(Sh)$ to Buffington's data, subject to the constraint $F \propto Sh^{3/2}$ when $Sh \gg Sh_{cr}$. There are different techniques for smoothly matching the low and high Shields number domains. This can be achieved, similarly to boundary layer corrections, by rescaling the variables:

$$\hat{q}_{ss} = \frac{\bar{q}_{ss}}{\bar{q}_{s*}} \quad \text{and} \quad \widehat{Sh} = \frac{Sh}{Sh_*}, \tag{B.3}$$

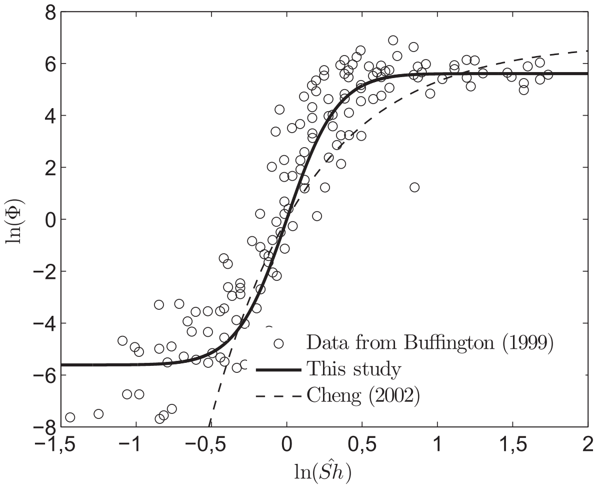

Fig. B.8. Comparison between the scaling factor $\Phi(\widehat{Sh})$ given by Eq. (B.5), the experimental data collected by Buffington [71], and Cheng's [82] equation.

where the pair $(Sh_*, \bar{q}_{s*})$ corresponds to the lower boundary of the domain over which Fernandez Luque and van Beek [56] interpolated their data. Fernandez Luque and van Beek [56] took $Sh_* \approx Sh_{cr} + 2 \times 10^{-3}$, but the precise value is unimportant as long as the point $(Sh_*, \bar{q}_{s*})$ lies on the curve associated with the bedload transport Eq. (B.2). Using nonlinear curve-fitting methods, we get:

$$\bar{q}_{ss}(Sh) = \frac{\bar{q}_{s*}\,Sh^{3/2}}{Sh_*^{3/2}}\,\Phi\left(\frac{Sh}{Sh_*}\right), \tag{B.4}$$

where,

$$\ln\Phi = 5.61 - 11.22\left[1 + \exp^{-37.41\,\ln\widehat{Sh}/(\ln^2\widehat{Sh} - 6.22)}\right]^{-1}, \tag{B.5}$$

Fig. B.8 shows Buffington's data, $\Phi(\widehat{Sh})$, and the trend $\bar{q}_{ss}/(V_s\,d) = 13\,Sh^{3/2}\exp(-0.05\,Sh^{-3/2})$ as fitted by Cheng [82] (with $\bar{q}_{s*}/(V_s\,d) = 10^{-4}$ and $Sh_* = 0.0376$). As desired, the function Φ (B.5) tends to the constant value 273.14 when $\widehat{Sh} > 2.72$, and so Eq. (B.4) is consistent with the scaling $\bar{q}_{ss} \propto Sh^{3/2}$ for the high Shields number domain. For $-0.5 < \ln\widehat{Sh} < 2$, the function Φ increases rapidly with increasing Sh, and it closely describes the experimental trend. Cheng's equation and our Eq. (B.5) show little difference in their predictions of $\bar{q}_{ss}$ for $\ln\widehat{Sh} > -0.5$. In contrast, for $\ln\widehat{Sh} < -0.5$, the equations behave quite differently since Eq. (B.5) leads to $\Phi \approx 0.0037$ in the limit $\widehat{Sh} \to 0$, whereas Cheng's equation shows that Φ becomes vanishingly small ($\ln\Phi \propto -Sh^{-3/2}$). Because of the fair amount of scatter in Buffington's data and the large fluctuations of the sediment transport rate, it is difficult to decide which one performs best.

We are now able to infer the steady-state particle activity $\langle\gamma\rangle_{ss}$ from $\bar{q}_{ss}$. Substituting Eq. (B.4) into Eq. (B.1) and using the Darcy–Weisback equation $\bar{v} = \sqrt{8/f}\,V_s\,Sh^{1/2}$, we end up with:

$$\langle\gamma\rangle_{ss} = \frac{\lambda}{\kappa} = \langle\gamma\rangle_*\,\widehat{Sh}\,\Phi(\widehat{Sh}), \quad \langle\gamma\rangle_* = \frac{\bar{q}_{s*}\sqrt{f}}{\beta\,V_s\sqrt{8\,Sh_*}}, \tag{B.6}$$

where $\langle\gamma\rangle_*$ is the ensemble-averaged particle activity for the reference point $(Sh_*, \bar{q}_{s*})$ ($\widehat{Sh} = 1$, $\Phi = 1$). The sediment-to-water velocity ratio β in Eq. (8) depends on the friction factor as $\beta \propto f^{1/2}$ [40] and so, in Eq. (B.6), $\langle\gamma\rangle_*$ is independent of the flow conditions. At large Shields numbers, we find the same scaling $\langle\gamma\rangle_{ss} \propto Sh$ as for Eq. (B.2). At small Shields numbers, $\langle\gamma\rangle_{ss}$ varies nonlinearly with the Shields number.

The scaling $\langle\gamma\rangle_{ss} \propto Sh$ was also obtained by Fernandez Luque and van Beek [56], Charru [59], and Lajeunesse et al. [76] at sufficiently high Shields numbers. Based on high-resolution particle tracking in flume experiments, Lajeunesse et al. [76] found $c_e/c_d = 1.75$ and $c_d = 0.094 \pm 0.006$ at moderate and high Shields numbers. Our Eq. (B.7) yields a constant ratio c_e/c_d for $Sh \gg Sh_*$, but as $Sh \to 0$, it predicts that this ratio varies nonlinearly with $\widehat{Sh}$:

$$\frac{c_e}{c_d} = \frac{\langle\gamma\rangle_*\,d^2}{Sh_*\,V_p}\,\Phi(\widehat{Sh}). \tag{B.7}$$

Appendix C. Calibration of the model parameters in Newton's experiment

Calibration was achieved in four steps.

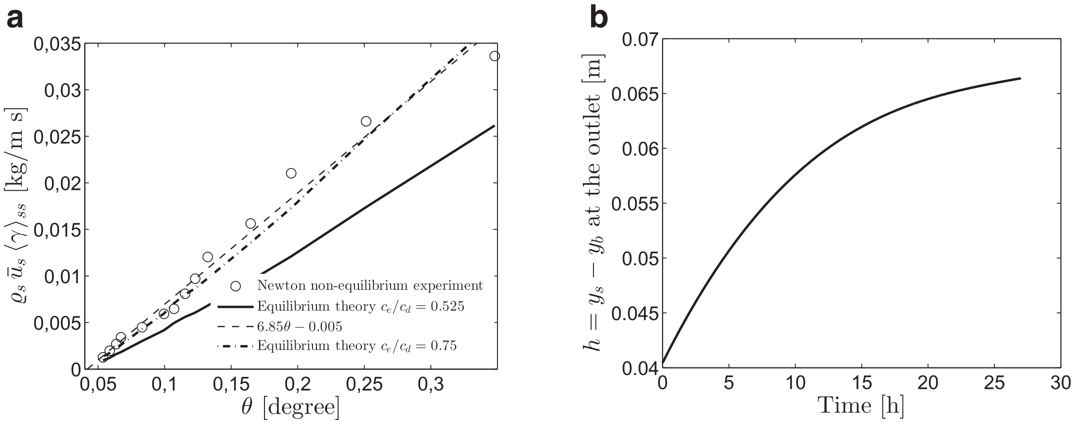

Fig. C.9. Calibration of the critical Shields number Sh_{cr} (or critical slope angle θ_{cr}) and the depth at the flume outlet in Newton's experiment. Both figures were constructed using available experimental data (see solid circles in Fig. 2) in the downstream reach of the flume ($x > 6$ m) with a constant water discharge $Q = 0.0057$ m^3 s^{-1} under uniform flow conditions. The parameter $Sh_{cr} = 0.0441$ is used in the numerical simulation to evaluate $\{\beta, \bar{u}_s\}$ and $\{\lambda, \langle\gamma\rangle_{ss}\}$ – see Eqs. (8) and (C.1), respectively. The dimensionless erosion-to-deposition ratio $c_e/c_d = 0.525$ was used in the non-equilibrium numerical simulation. There was good agreement with the experimental results when the sediment diffusion was included in the modeling, as shown in Fig. 2. Plot (b) was obtained by solving Eqs. (10) and (4) for h and by varying the slope $\tan\theta$ with time as per the experiments.

1. The initial water depth H, bed angle θ, and water discharge Q were used to calibrate the bed roughness scaling factor k_s for the determination of the Darcy–Weisbach friction factor f, which takes the form (4) in a fully developed turbulent flow and rough regime. On substituting Eq. (4) into Eq. (10) and solving for the scaling factor, we got $k_s \approx 4$, which was kept constant during the numerical simulations. Following Bohorquez and Ancey [40], we computed the sediment velocity using Eq. (8). Note that during the numerical simulations, the parameter δ^2 increased due to the greater flow depths developing at shallower slopes as time elapsed, modifying both f and β [see Eqs. (4) and (8)].
2. Then, we calibrated the critical Shields number Sh_{cr} for the onset of sediment motion by fitting the solid discharge at the flume outlet [circles in Fig. 2(c)] as a function of the mean bed slope [corresponding to the experimental bed in Fig. 2(a)], which gave $\bar{q}_{ss} = 6.85\,\theta - 0.005$, with θ in degrees and $\bar{q}_{ss}$ in m^2 s^{-1}. This step required algebraical manipulations and iterations of the equations, which are not reported here for the sake of brevity. The critical angle of equilibrium was thus $\theta_{cr} = 0.042°$. Taking into account that Newton's experiment kept the water discharge constant, and making use of (10), (11), and (4), we got the critical Shields number $Sh_{cr} = 0.0441$ for the theoretical grain-size to water-depth ratio $\delta^2 = 0.009$.
3. The next parameter to be calibrated was the erosion/deposition rate $\kappa = c_d\sqrt{(s-1)\,g/d}$ or, equivalently, the dimensionless parameter c_d [40]. To be consistent with previous non-equilibrium numerical simulations of Newton's degradation experiment [14,17], we estimated the deposition rate from the convective adaptation length ℓ_c as $\kappa = \bar{u}_s/\ell_c$. Using the scaling proposed by Charru [59] for turbulent flows, we obtained $c_d = \bar{u}_s\sqrt{d}/\sqrt{(s-1)\,g\,\ell_c^2}$. Wu and Wang [14], El kadi Abderrezzak and Paquier [17], and Zhang et al. [15] adopted $\ell_c \approx 1$ m. Surprisingly, by setting $\ell_c \sim 1$ m, we got $c_d \sim O(10^{-3})$ in Newton's experiment—a much lower value than the $c_d = 0.1$ proposed by Lajeunesse et al. [76]. We set $c_d = 1.6 \times 10^{-3}$ in our computations.
4. Following Charru [59] and Bohorquez and Ancey [40], we set the entrainment rate λ so that particle activity reached a steady state during the simulation:

$$\langle\gamma\rangle_{ss} = \frac{\lambda}{\kappa} = \frac{c_e\,V_p}{c_d\,d^2}\,(Sh - Sh_{cr})\,. \tag{C.1}$$

Fig. C.9(a) shows a comparison between the sediment transport rate in Newton's experiments and our theoretical prediction for uniform flow with $c_e = 8.4 \times 10^{-4}$. For this value of c_e, theory underestimates the experimental bedload transport rate in non-equilibrium degradation experiments. This is not a shortcoming of non-equilibrium transport theory, but rather this apparently odd behavior reflects the increase in the total sediment load transport rate due to sediment diffusion and an unsteady flow, as described in Section 3.2.

Appendix D. Dispersion relation and Briggs–Bers criterion

The solution to the linear perturbation equations in the spatio-temporal stability analysis can be written as $(z', \phi', \eta', u') = \overline{T}\exp[i(k\hat{x} - \omega\hat{t})]$, where the eigenvector is denoted by $\overline{T} \equiv (\zeta, \Phi, \Gamma, U)$, the complex wavenumber by $k = k_r + i\,k_i$, and the complex frequency by $\omega = \omega_r + i\,\omega_i$.

For the closure Eq. (B.2), the eigenvalues and eigenvectors were obtained from the following generalized eigenproblem $\overline{\overline{A}} \cdot \overline{T} = 0$:

$$\left[-i\,\omega \begin{pmatrix} 1 & 0 & 0 \\ 0 & 1 & 0 \\ 0 & 0 & Fr^2 \end{pmatrix} + i\,k \begin{pmatrix} \beta & 0 & \beta \\ 0 & 1 & 1 \\ \frac{i\,k_e}{\omega} & 1 & Fr^2 - \frac{i\,2\,k_e}{\omega\,(1-u_*^2)} \end{pmatrix} - k^2 \begin{pmatrix} -\mathcal{D} & 0 & 0 \\ 0 & 0 & 0 \\ 0 & 0 & -\mathcal{V} \end{pmatrix} + \begin{pmatrix} k_d & 0 & -\frac{2\,k_d}{1-u_*^2} \\ 0 & 0 & 0 \\ 0 & -1 & 2 \end{pmatrix} \right] \cdot \begin{bmatrix} \Phi \\ \Gamma \\ U \end{bmatrix} = 0. \tag{D.1}$$

The dimension of matrix (D.1) was reduced by one using $\zeta = i\,k_e\,\Phi/\omega - i\,2\,k_e\,U/[\omega\,(1-u_*^2)]$. The solution was controlled by the following dimensionless groups:

$$k_e = \frac{\pi\,c_e(1-u_*^2)}{6\,(1-\zeta_b)\,\delta\,Fr\sqrt{s-1}}, \quad k_d = \frac{c_d(s-1)}{\delta\,Fr\,\tan\theta}, \quad u_* = \sqrt{\frac{Sh_{cr}}{Sh}}, \quad \mathcal{V} = \nu_t\,Fr\,(\tan\theta)^{3/2}, \quad \mathcal{D} = \frac{D_u\,\tan\theta}{H\,V}. \tag{D.2}$$

The dispersion relation was obtained by setting the determinant of (D.1) to zero, *i.e.*, $\mathbb{D}(k,\omega) \equiv |\overline{\overline{A}}| = 0$. The dispersion relation links the complex wavenumber k with the complex frequency ω. Note that the dimensionless particle diffusion $\mathcal{D}$ increases the order of the characteristic polynomial (D.1) up to $O(k^2)$.

For determining the saddle points, we sought solutions to $\mathbb{D}(k_0,\omega_0) = 0$ and $\partial_k\mathbb{D}(k_0,\omega_0) = 0$, with $\partial_{kk}\mathbb{D}(k_0,\omega_0) \neq 0$ resulting from a pinch point between two spatial branches $k^+(\omega)$ and $k^-(\omega)$ originating from distinct halves of the k-plane with $k_{0,\,i} < 0$ (*i.e.*, spatially growing solution) and $\omega_{0,\,i} > 0$ (*i.e.*, temporal growing solution). In doing so, we ensured the zero group velocity condition $c_g = \partial\omega/\partial k = (\partial\mathbb{D}/\partial k)/(\partial\mathbb{D}/\partial\omega) = 0$, referred to as the Briggs–Bers or (in Soviet literature) the Fainberg–Kurilko–Shapiro criterion [68,69]. Under this condition, the flow is absolutely unstable. Note that the increase to $O(k^2)$ in the order of the characteristic polynomial (D.1) occurs with $\mathcal{D} > 0$ and favors the existence of mathematical solutions to the Briggs–Bers condition. In the presence of absolute instability, with just one saddle point, there are an absolute frequency and an absolute growth rate that determine the system's selective response to perturbations. The system therefore selects a natural frequency and, consequently, a unique saddle point wavenumber for the spatial branches among the wide range of unstable wavenumbers k. In this case, the response is dominated by the mode with zero group velocity which grows in the same place, whereas the rest of the frequencies and wavenumbers are swept away by the flow [59]. In the presence of multiple saddle points, Pier and Peake [83] showed that the theoretical calculation of the natural frequency and wavenumber is much more complicated.

References

[1] W. Wu, Computational River Dynamics, Taylor & Francis, London, 2007.
[2] E. Meyer-Peter, R. Müller, Formulas for bed load transport, in: Proceedings of the Second Meeting of the International Association for Hydraulic Structures Research, International Association for Hydraulic Research, Delft, Netherlands, 1948, pp. 39–64.
[3] P. Ackers, W.R. White, Sediment transport: New approach and analysis, J. Hydraul. Div. Am. Soc. Civ. Eng. 99 (1973) 2041–2060.
[4] G. Parker, Surface-based bedload transport relation for gravel rivers, J. Hydraul. Res. 28 (1990) 417–436.
[5] A. Recking, F. Liébault, C. Peteuil, T. Jolimet, Testing bedload transport equations with consideration of time-scales, Earth Surf. Process. Landf. 37 (2012) 774–789.
[6] H.A. Einstein, Bedload transport as a probability problem, Mitt. Versuchsanst. Wasserbau Eidg. Tech. Hochsch, Zürich; Switzerland, 1937. (PhD thesis).
[7] B.C. Phillips, A.J. Sutherland, Spatial lag effects in bed load sediment transport, J. Hydraul. Res. 427 (1989) 115–133.
[8] S.C. Jain, Note on lag in bedload discharge, J. Hydraul. Eng. 118 (1992) 904–917.
[9] F. Charru, Selection of the ripple length on a granular bed sheared by a liquid flow, Phys. Fluids 18 (2006) 121508.
[10] M. Guan, N.G. Wright, P.A. Sleigh, Multimode morphodynamic model for sediment-laden flows and geomorphic impacts, J. Hydraul. Eng. 141 (2015) 04015006.
[11] H. Qian, Z. Cao, G. Pender, H. Liu, P. Hu, Well-balanced numerical modelling of non-uniform sediment transport in alluvial rivers, Int. J. Sediment Res. 30 (2015) 117–130.
[12] Z. Cao, G. Pender, S. Wallis, P.A. Carling, Computational dam-break hydraulics over erodible bed, J. Hydraul. Eng. 130 (2004) 689–703.
[13] P. Bohorquez, R. Fernandez-Feria, Transport of suspended sediment under the dam-break flow on an inclined plane bed of arbitrary slope, Hydrol. Process. 22 (2008) 2615–2633.
[14] W. Wu, S.S.Y. Wang, One-dimensional explicit finite-volume model for sediment transport, J. Hydraul. Res. 46 (2008) 87–98.
[15] S. Zhang, J.G. Duan, M. Strelkoff, Grain-scale non-equilibrium sediment-transport model for unsteady flow, J. Hydraul. Eng. 139 (2013) 22–36.
[16] Z. Cao, R. Day, S. Egashira, Coupled and decoupled numerical modeling of flow and morphological evolution in alluvial rivers, J. Hydraul. Eng. 128 (2002) 306–321.
[17] El Kadi Abderrezzak, A. Paquier, One-dimensional numerical modeling of sediment transport and bed deformation in open channels, Water Resour. Res. 45 (2009) W05404.
[18] G. Parker, Y. Fukushima, H.M. Pantin, Self-accelerating turbidity currents, J. Fluid Mech. 171 (1986) 145–181.
[19] B. Greimann, Y. Lai, J. Huang, Two-dimensional total sediment load model equations, J. Hydraul. Eng. 134 (2008) 1142–1146.
[20] N.J. Balmforth, A. Vakil, Cyclic steps and roll waves in shallow water flow over an erodible bed, J. Fluid Mech. 695 (2012) 35–62.
[21] V. Nikora, H. Habersack, T. Huber, I. McEwan, On bed particle diffusion in gravel bed flows under weak bed load transport, Water Resour. Res. 38 (2002) WR000513.
[22] V. Ganti, M.M. Meerschaert, E. Foufoula-Georgiou, E. Viparelli, G. Parker, Normal and anomalous dispersion of gravel tracer particles in rivers, J. Geophys. Res. 115 (2010) F00A12.
[23] R.L. Martin, D.J. Jerolmack, R. Schumer, The physical basis for anomalous diffusion in bed load transport, J. Geophys. Res. 117 (2012) F01018.
[24] J.C. Roseberry, M.W. Schmeeckle, D.J. Furbish, A probabilistic description of the bed load sediment flux: 2. Particle activity and motions, J. Geophys. Res. 117 (2012) F03032.

[25] J. Heyman, H.B. Ma, F. Mettra, C. Ancey, Spatial correlations in bed load transport: Evidence, importance, and modeling, J. Geophys. Res. Earth Surf. 119 (2014) 1751–1767.
[26] G. Seizilles, E. Lajeunesse, O. Devauchelle, M. Bak, Cross-stream diffusion in bedload transport, Phys. Fluids 26 (2014) 013302.
[27] J. Campagnol, A. Radice, F. Ballio, V. Nikora, Particle motion and diffusion at weak bed load: accounting for unsteadiness effects of entrainment and disentrainment, J. Hydraul. Res. 63 (2015) 633–648.
[28] H. Sun, D. Chen, Y. Zhang, L. Chen, Understanding partial bed-load transport: Experiments and stochastic model analysis, J. Hydrol. 521 (2015) 196–204.
[29] J. Heyman, P. Bohorquez, C. Ancey, Dynamics of bed load particles in super-critical flows at the onset of motion, *submitted to* J. Geophys. Res.: Earth Surf. (2016).
[30] T.G. Drake, R.L. Shreve, W.E. Dietrich, L.B. Leopold, Bedload transport of fine gravel observed by motion-picture photography, J. Fluid Mech. 192 (1988) 193–217.
[31] K. Ramos, S. Gibson, L. Kavvas, R. Heath, J. Sharp, Estimating bed-load advection and dispersion coefficients with the method of moments, in: K. Karvazy, V.L. Webster (Eds.), World Environmental and Water Resources Congress 2015: Floods, Droughts, and Ecosystems, ASCE, Baltimore, 2015, pp. 1736–1741.
[32] W.E.H. Culling, Analytical theory of erosion, J. Glaciol. 68 (1960) 336–344.
[33] C. Paola, Quantitative models of sedimentary basin filling, Sedimentology 47 (2000) 121–178.
[34] D.J. Furbish, P.K. Haff, From divots to swales: Hillslope sediment transport across divers length scales, J. Geophys. Res. 115 (2010) F03001.
[35] A.M. Heimsath, D.J. Furbish, W.E. Dietrich, The illusion of diffusion: Field evidence for depth-dependent sediment transport, Geology 33 (2005) 949–952.
[36] T. Salles, G. Duclaux, Combined hillslope diffusion and sediment transport simulation applied to landscape dynamics modelling, Earth Surf. Process. Landf. 40 (2015) 823–839.
[37] D.J. Furbish, P.K. Haff, J.C. Roseberry, M.W. Schmeeckle, A probabilistic description of the bed load sediment flux: 1. Theory, J. Geophys. Res. 117 (2012) F03031.
[38] C. Ancey, J. Heyman, A microstructural approach to bed load transport: mean behaviour and fluctuations of particle transport rates, J. Fluid Mech. 744 (2014) 129–168.
[39] C. Ancey, P. Bohorquez, J. Heyman, Stochastic interpretation of the advection diffusion equation and its relevance to bed load transport, J. Geophys. Res. Earth Surf. 120 (2015) 2529–2551.
[40] P. Bohorquez, C. Ancey, Stochastic-deterministic modeling of bed load transport in shallow water flow over erodible slope: Linear stability analysis and numerical simulation, Adv. Water Resour. 83 (2015) 36–54.
[41] S. Zhang, J.G. Duan, 1D finite volume model of unsteady flow over mobile bed, J. Hydrol. 405 (2011) 57–68.
[42] J. Wainwright, A.J. Parsons, J.R. Cooper, P. Gao, J.A. Gillies, L. Mao, J.D. Orford, P.G. Knight, The concept of transport capacity in geomorphology, Rev. Geophys. 53 (2015) 1155–1202.
[43] N.S. Cheng, Y.M. Chiew, Analysis of initiation of sediment suspension from bed load, J. Hydraul. Eng. 125 (1999) 855–861.
[44] C.T. Newton, An experimental investigation of bed degradation in an open channel, Trans. Boston Soc. Civ. Eng. 195 (1951) 28–60.
[45] H.H. Cao, Resistance Hydraulique d'un lit à Gravier Mobile à Pente raide; étude Expérimentale, EPFL, Switzerland, 1985 (Ph.D. thesis). http://dx.doi.org/10.5075/epfl-thesis-589.
[46] J.C. Bathurst, W.H. Graf, H.H. Cao, Bedload discharge equations for steep mountain rivers, in: C.R. Thorne, J.C. Bathurst, R.D. Hey (Eds.), Sediment Transport Equations in Gravel-Bed Rivers, Wiley, Chichester, 1987, pp. 453–491.
[47] A. Recking, V. Bacchi, M. Naaim, P. Frey, Antidunes on steep slopes, J. Geophys. Res. 114 (2009) F04025.
[48] F. Mettra, Morphodynamic Mechanisms in Steep Channels: From Local Processes to Large-Scale Evolution, EPFL, Switerzland, 2014 (Ph.D. thesis). http://dx.doi.org/10.5075/epfl-thesis-6065.
[49] M.H. García, Sediment transport and morphodynamics, in: M.H. García (Ed.), Sedimentation Engineering, ASCE Manuals and Reports on Engineering Practice 110, American Society of Civil Engineers, Reston, 2007, pp. 21–164.
[50] Z. Cao, P. Hu, K. Hu, G. Pender, Q. Liu, Modelling roll waves with shallow water equations and turbulent closure, J. Hydraul. Res. 53 (2015) 161–177.
[51] P.Y. Julien, Erosion and Sedimentation, second ed., Cambridge University Press, Cambridge, 2010.
[52] C. Ancey, A.C. Davison, T. Böhm, M. Jodeau, P. Frey, Entrainment and motion of coarse particles in a shallow water stream down a steep slope, J. Fluid Mech. 595 (2008) 83–114.
[53] C. Ancey, Stochastic modeling in sediment dynamics: Exner equation for planar bed incipient bed load transport conditions, J. Geophys. Res. 115 (2010) F00A11.
[54] D.J. Furbish, A.E. Ball, M.W. Schmeeckle, A probabilistic description of the bed load sediment flux: 4. Fickian diffusion at low transport rates, J. Geophys. Res. 117 (2012) F03034.
[55] F. Ballio, V. Nikora, S.E. Coleman, On the definition of solid discharge in hydro-environment research and applications, J. Hydraul. Res. 52 (2014) 173–184.
[56] Fernandez Luque, R. van Beek, Erosion and transport of bed-load sediment, J. Hydraul. Res. 14 (1976) 127–144.
[57] D.I. Ketcheson, M. Parsani, R.J. LeVeque, Higher order wave propagation algorithms for hyperbolic systems, SIAM J. Sci. Comput. 35 (2013) A351–A377.
[58] S. Gottlieb, D.I. Ketcheson, C.W. Shu, High order strong stability preserving time discretizations, J. Sci. Comput. 38 (2009) 251–289.
[59] F. Charru, Hydrodynamic Instabilities, Cambridge University Press, Cambridge, 2011.
[60] A.J. Bagnold, The movement of desert sand, Proc. R. Soc. Lond. Ser. A 157 (1936) 594–620.
[61] M.S. Yalin, A.M.F. da Silva, Fluvial Processes, IAHR Monograph, IAHR, Delft, The Netherlands, 2001.
[62] R. Courant, K. Friedrichs, H. Lewy, On the partial difference equations of mathematical physics, IBM Journal of Research and Development 11 (1967) 215–234.
[63] R.J. LeVeque, Finite Volume Methods for Hyperbolic Problems, Cambridge University Press, Cambridge, 2002.
[64] E. Blayo, L. Debreu, Revisiting open boundary conditions from the point of view of characteristic variables, Ocean Model. 9 (2005) 231–252.
[65] D.A. Vieria, W. Wu, CCHE1D Version 3. 0 - Model Capabilities and Applications, Technical Report No. NCCHE-TR-2002-05, National Center for Computational Hydroscience and Engineering, 2002.
[66] J.B. Abril, M.S. Altinakar, W. Wu, One-dimensional numerical modelling of river morphology processes with non-uniform sediment, in: R. Murillo Muñoz (Ed.), River Flow 2012 - Proceedings of the International Conference on Fluvial Hydraulics, vol. 1, CRC Press, Taylor & Francis, 2012, pp. 529–535.
[67] A.G. Davies, L.C. van Rijn, J.S. Damgaard, J. van de Graaff, J.S. Ribberink, Intercomparison of research and practical sand transport models, Cost Eng. 46 (2002) 1–23.
[68] P.J. Schmid, D.S. Henningson, Stability and Transition in Shear Flows, Springer, 2001.
[69] M.P. Juniper, A. Hanifi, V. Theofilis, Modal stability theory, Appl. Mech. Rev. 66 (2014) 024804.
[70] N.J. Balmforth, A. Provenzale, Patterns of dirt, in: N.J. Balmforth, A. Provenzale (Eds.), Geomorphological Fluid Mechanics, Springer Verlag, Berlin, 2001, pp. 369–393.
[71] J. Buffington, The legend of A. Shields, J. Hydraul. Eng. 125 (1999) 376–387.
[72] J.W. Lavelle, W.C. Thacker, A pretty good sponge: Dealing with open boundaries in limited-area ocean models, Ocean Model. 20 (2008) 270–292.
[73] F.M. Exner, Ueber die Wechselwirkung zwischen Wasser und Geschiebe in Fluessen, Sitzungsberichte der kaiserlichen Akademie der Wissenschaften Wien, Abteilung IIa 134 (1925) 165–205.
[74] J. Li, M. Qi, Local scour induced by upstream riverbed level lowering, Nat. Hazards 77 (2015) 1811–1827.
[75] Z. Cao, Z. Li, G. Pender, P. Hu, Non-capacity or capacity model for fluvial sediment transport, Water Manag. 165 (2010) 193–211.

[76] E. Lajeunesse, L. Malverti, F. Charru, Bed load transport in turbulent flow at the grain scale: Experiments and modeling, J. Geophys. Res. 115 (2010) F04001.
[77] A.A. Kassem, H.M. Chaudhry, Comparison of coupled and semi-coupled numerical models for alluvial channel, J. Hydraul. Eng. 124 (1998) 794–802.
[78] C. Ancey, T. Böhm, M. Jodeau, P. Frey, Statistical description of sediment transport experiments, Phys. Rev. E 74 (2006) 011302.
[79] J.F. Kennedy, The formation of sediment ripples, dunes, and antidunes, Annu. Rev. Fluid Mech. 1 (1969) 147–168.
[80] J.F. Kennedy, Stationary Waves and Antidunes in Alluvial Channel, Caltech, Pasadena, 1960 (Ph.D. thesis).
[81] C.W. Gardiner, M.L. Steyn-Ross, Adiabatic elimination in stochastic systems. II. Application to reaction diffusion and hydrodynamic-like systems, Phys. Rev. A 29 (1984) 2823.
[82] N. Cheng, Exponential formula for bedload transport, J. Hydraul. Eng. 128 (2002) 942–946.
[83] B. Pier, N. Peake, Global modes with multiple saddle points, Eur. J. Mech. B Fluids 49 (2015) 335–344.